INTEGRATED PHOTONICS

A Dissertation

Presented to the Faculty of the Graduate School

of Cornell University

in Partial Fulfillment of the Requirements for the Degree of

Doctor of Philosophy

by

Alexander A. Gondarenko

February 2010

INTEGRATED PHOTONICS

Alexander A. Gondarenko, Ph.D.

Cornell University 2010

In 1958 the first integrated circuit was demonstrated to combine transistors, resistors, and capacitors [36]. To this date fabrication technology has been driven by the growing demand for monolithically constructed, densely packed electronic components. The exponentially shrinking device size decreased the feature dimensions from 10 microns to 32 nm and grew transistor count from 2,300 to over 2,000,000,000 in Intel's 4004 and Intel Kentsfield XE microprocessors. The benefits of micro- and nano-fabrication was not limited to just computer chips. MEMs, spintronic, microfluidics, and integrated photonics were all made possible by the ever expanding ability to form complex geometries, on a wide variety of materials, on a micron and submicron scale.

This dissertation is part of an effort to design and fabricate novel integrated photonic devices compatible with standard electron beam and photo lithography and utilize a readily available material base. We aim to create devices with a decreased footprint on a chip and operate in the infrared, visible, and UV spectra. We present two general sections, the first is a theoretical effort to find the fundamental design geometries for a variety of optical problems. The second section is an experimental demonstration of techniques and devices for novel optical phenomena in an integrated package.

In the theoretical section we develop and apply computational evolutionary algorithms to explore problems of light confinement, coupling, and guiding in two and three dimensional device geometries. Our general aim is to find a

global limit to optimal device geometry and performance given a set of constrains. Experimentally, we demonstrate an efficient design and a fabrication process for a short development cycle of photonic devices. For the design part of the workflow, we develop a computational approach to explore device geometries with minimum initial assumptions for a variety of photonic problems. For the fabrication part of the workflow, we optimize dielectric deposition, electron beam lithography, resist post processing, etching, and cladding to yield low loss photonic devices in silicon nitride. We measure the propagation losses in our devices and demonstrate their origin. We also design and test cavities to demonstrate novel nonlinear optical phenomena.

BIOGRAPHICAL SKETCH

Alexander A. Gondarenko was born in Karaganda, USSR in 1982. He received an Optics BS, Computer Science BS and Mathematics BA from University of Rochester, Rochester, NY in 2004.

To my mother and father.

ACKNOWLEDGEMENTS

This part of my thesis is most significant and least likely to ever be fully finished. There are too many people who have helped and assisted me in the course of my research and education to able to remember.

First and foremost, I would like to thank my research advisor, Professor Michal Lipson. Her kindness and indispensable energy has never ceased to motivate and amaze me. I thank her for providing all the resources a student could ever ask for, and for her patience with all of my tangent ideas through the years. Her thoroughness and rigor in editing manuscripts has helped me tremendously. I would like to thank Professor Farhan Rana for his piercing insight into all of the questions I brought to him, for his guidance and his insightful courses. I also want thank Professor Alex Gaeta for his insight and input in my research.

Without the fabrication assistance, encyclopedic knowledge and late hours of Dr. Rob Ilic my progress in fabrication could not have occurred. I look forward to late night discussions with him in the cleanroom for years to come in my future research. I am grateful to the entire CNF staff for their assistance in fabrication. I would especially like to thank Meredith Metzler for his help and training on a lot of the tools.

Prof. Lipson has assembled a group without which my experience in Cornell would have been far more limited. The social and friendly environment has always catalyzed new ideas with people working on vastly different projects. At the same time, the general research theme in the group always fostered assistance from more experienced members to the beginning ones. Without such an environment, much of the knowledge within the group about the constantly changing laboratory and nuances of the cleanroom, which change al-

most weekly, would not be possible. I would like to thank Dr. Brad Schmidt and Dr. Jagat Shakya for their limitless assistance in the beginning of my research. I would like to thank Linnell Martinez for his assistance in fabrication.

The morale of the group would never have reached its peaks without Dr. Jacon Robinson, whose organization of the group extracurriculars has been missed since he left. I would like to thank Nick Sherwood for his will and ability to humor my tangent research directions.

I would like to thank Dr. Jaime Cardenas and his wife Cecilia Cardenas for helping me in proofreading of this thesis. I would like to especially thank Dr. Christina Manolatou for her assistance in my computational work.

I would also like to thank for help, assistance, and insight from Dr. Danilo Spadoti, Dr. Gustavo Wiederhecker, Dr. Po Dong, Dr. Carl Poitras, Dr. Amy Turner-Foster, Dr. Mark Foster, Dr. Long Chen, Arthur Nitkowzki, Stefan Preble, Biswajeet Guha, Lucas Gabrielli, Lian-Wee Luo, Debo Olaosebikan, Hugo Lira, Kyle Preston, Sasikanth Manipatruni, Jacob S. Levy and Bernardo Kyotoku. Just the thought of listing their names brings sadness leaving such a large, friendly, and helpful group.

I would also like to thank my friends outside of the group for their support: Dr. Dana Weinstein, Rick James Brown, Katarzhyna Bryc, Caitlin Stern, Caitling Cuningham, Jessy Barker, Kat Agres, Kathy King, Steve Raciti, Molly Pucci, Erica Pollock, Christina Block, Amanda Schlenker, Tien Tran and Peter Rasmussen.

TABLE OF CONTENTS

LIST OF FIGURES

CHAPTER 1

INTRODUCTION

1.1 Integrated Photonics

The ability to fabricate wavelength scale structures out of materials transparent in the ultraviolet, visible, and infra red spectrum allows for creation of a wide variety of compact passive and active optical devices. Passive devices like waveguides, gratings, and filters and active devices like lasers, detectors, and modulators have been demonstrated on different integrated platforms. The small size of these devices and high confinement of light allows for strong light matter interaction and allows for fast operation and low power consumption. The field of science and engineering which deals with manipulation of light on the wavelength scale is known as photonics.

Progress in photonics has allowed for devices used in the telecommunication industry to be compact and moderately power efficient. Nevertheless the sheer size of optical networks worldwide consumes a significant amount of energy. The continuous growth of telecommunication industry has been doubling in size every 14 months[1]. If this trend continues without significant changes in the power efficiencies of photonic technology, we will be using more energy for telecommunication than any other single industry [17].

Many of the photonic devices use cavities to temporally and spatially confine light. Strong light confinement enhances light matter interaction, can decrease the necessary active volume of a device, and reduce energy consumption

[1]Capacity-Distance product is used as the measurement metric

in active devices. Hence, it is of vital importance from scientific and engineering standpoints to control light confinement of wavelength and sub wavelength scales.

CHAPTER 2

COMPUTATIONAL ALGORITHMS

2.1 Evolutionary Algorithms

Evolutionary algorithms (EAs) are inspired by natural evolution and operate by repeatedly selecting, varying, and replicating successful individuals in a population of candidate solutions [30, 52, 40]. These algorithms are well suited for finding solutions to problems that involve very large and complex search spaces with little formal knowledge about the location of optima or smooth gradients leading to them. In particular, EAs are well suited for searching open-ended design spaces that are not characterized by a small set of parameters that can be optimized, but are spanned instead by an unbounded set of functional geometries [44].

In general EA are stochastic optimization algorithms. For a given merit function $F(x_1...x_n)$ over a many dimensional space, we seek to find a global maximum. The algorithm starts with a random set of solutions S of size k and evaluates F for each element in S. The solutions are sorted by their merit values, and a bottom fraction of the solutions are immediately discarded. The solution set is repopulated with a new set of x vectors by selecting a pair of existing elements from S, performing a randomized merge operation on them, and a sequence of random perturbations. The new solutions in S are evaluated by the merit function and the sorting, discarding, and repopulating cycle is repeated until some steady state in the maximum merit value is found.

Typically evaluation of the merit function is the only computationally inten-

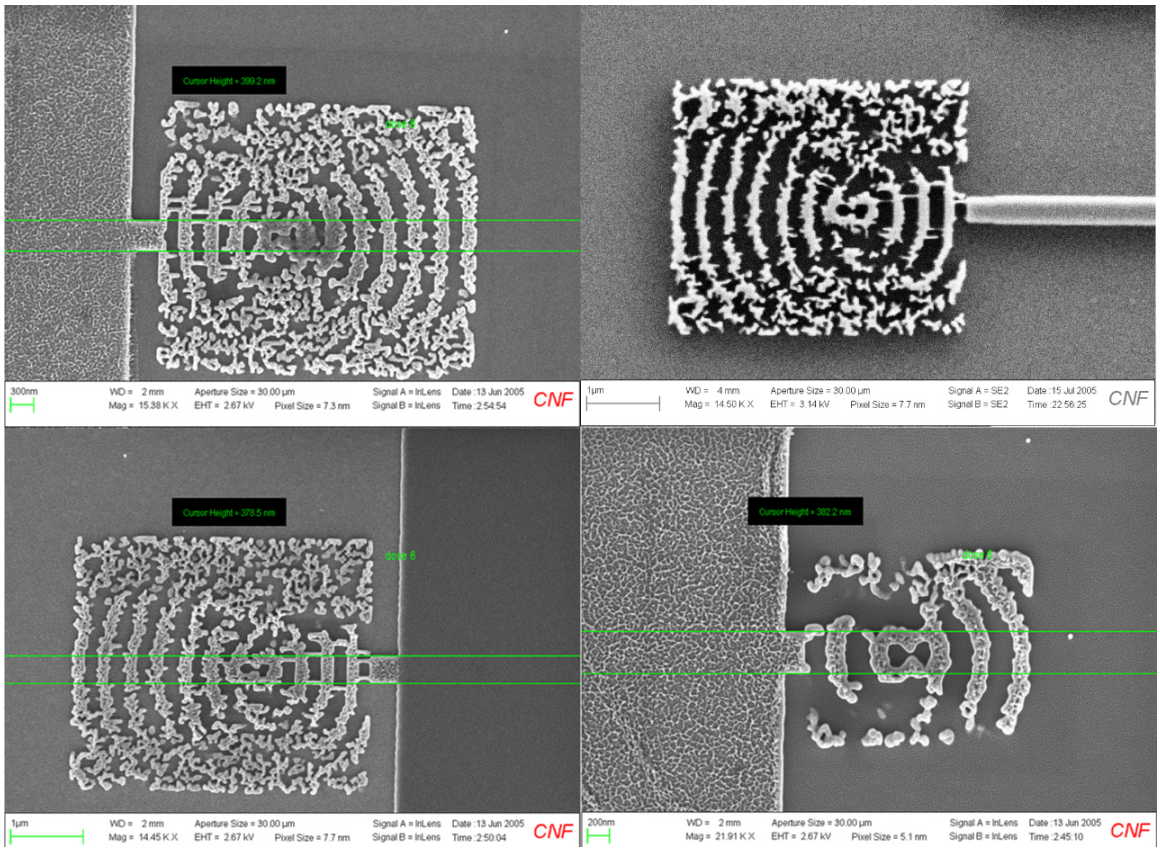

Figure 2.1: Micrographs of a photonic device for localization of light fabricated in silicon.

sive step in the algorithm. Since each element of a solution is evaluated separately, the algorithm is innately parallel. Several computers can evaluate the solution set with minimal communication requirement. This allows EA evaluation time to scale perfectly with the number of computing nodes available as long as the number of computing nodes is equal to or less than the size of the solution set.

2.2 Finite Difference Time Domain Algorithm

Finite-difference time-domain is a common computational electrodynamics modeling algorithm. It is relatively simple to implement in software and since it is a time domain algorithm, the solutions can cover a wide frequency range from a single simulation run. The basic algorithm was first demonstrated in 1966 by Kane Yee [81]. Since their first realization, FDTD techniques have been used to model electromagnetic radiation anywhere from ultra low frequency in geophysics involving the entire Earth ionosphere to visible light frequencies [67, 25]. Most generally, FDTD is a grid based differential time domain numerical modeling method. The partial differential form of Maxwell's equations is discretized with a central difference approximation. In cartesian coordinates Maxwell's equations can be written as a set of scalar equations:

$$\begin{aligned} -\frac{\partial B_x}{\partial t} &= \frac{\partial E_z}{\partial y} - \frac{\partial E_y}{\partial z} \\ -\frac{\partial B_y}{\partial t} &= \frac{\partial E_x}{\partial z} - \frac{\partial E_z}{\partial x} \\ \frac{\partial B_z}{\partial t} &= \frac{\partial E_x}{\partial y} - \frac{\partial E_y}{\partial x} \end{aligned} \tag{2.1}$$

$$\begin{aligned} \frac{\partial D_x}{\partial t} &= \frac{\partial H_z}{\partial y} - \frac{\partial H_y}{\partial z} \\ \frac{\partial D_y}{\partial t} &= \frac{\partial H_x}{\partial z} - \frac{\partial H_z}{\partial x} \\ \frac{\partial D_z}{\partial t} &= \frac{\partial H_y}{\partial x} - \frac{\partial H_x}{\partial y} \end{aligned} \tag{2.2}$$

yielding two sets of equations for electric and magnetic fields. We denote a grid point in space in time and denote a function of space time as,

$$F(\imath\Delta x, \imath\Delta y, \imath\Delta z, n\Delta t) = F^n(i, j, k). \tag{2.3}$$

From the scalar equations 2.1 and 2.2 we write finite difference equations:

$$\frac{B_x^{n+1/2}(i, j+1/2, k+1/2) - B_x^{n-1/2}(i, j+1/2, k+1/2)}{\Delta t} = \tag{2.4}$$

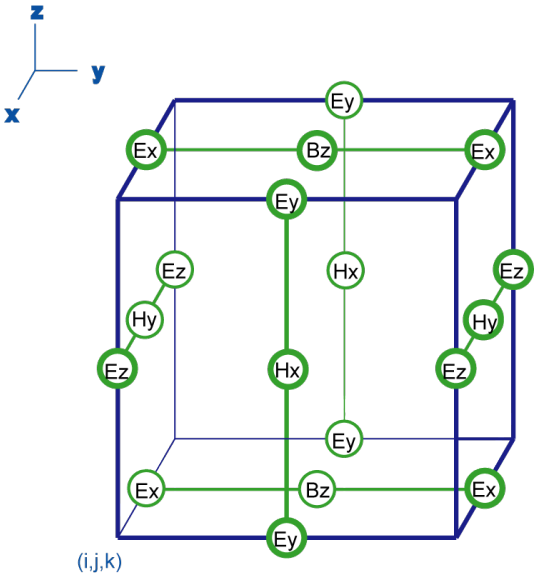

Figure 2.2: Positions of different field components in Yee's finite difference time domain algorithm scheme. The electric field components lie in the middle of edges, and the magnetic field components are in the center of faces.

$$\frac{E_y^n(i,j+1/2,k+1)-E_y^n(i,j+1/2,k)}{\Delta z}- \frac{E_z^n(i,j+1,k+1/2)-E_z^n(i,j,k+1/2)}{\Delta y}$$

$$\frac{D_x^{n+1/2}(i,j+1/2,k+1/2)-D_x^{n-1/2}(i,j+1/2,k+1/2)}{\Delta t} = \frac{H_y^{n-1/2}(i+1/2,j+1/2,k)-H_y^{n-1/2}(i+1/2,j-1/2,k)}{\Delta y}- \frac{H_z^{n-1/2}(i+1/2,j,k+1/2)-H_z^{n-1/2}(i+1/2,j,k-1/2)}{\Delta z}, \tag{2.5}$$

where equations for B_y, B_z, E_y and E_z can be similarly computed. The grid positions are shown in Fig. 2.2.

The equations for electric and magnetic fields are computed alternatively yielding respective fields evolving over $\Delta t/2$ steps in time. Computing field propagation in three dimensions consume a significant amount of time as the

size of the grid increases. Fortunatley FDTD lends itself to efficient parallelization. The spatial volume can be subdivided into smaller chunks and a separate CPU can be assigned to each chunk. Every time an equation is evaluated over a subvolume by a CPU, it must exchange values at the edges of its sub domain to continue to the next iteration. Hence, dividing the computational volume between many computers and providing an efficient communication medium between them allows for an almost linear speedup with number of computing nodes. The linearity of the speedup directly depends on the quality of the interconnect mesh between computing nodes. For optimal performance a low latency optical interconnect is typically used.

2.3 Application to Photonic Problems

EAs have been shown to be an effective method for solving problems in photonics. They have been applied to design waveguide and photonic crystal based spot-size converters [59, 66], photonic crystals [56, 64], polarization converters [14], fiber Bragg gratings [48], difference frequency generation based wavelength conversion [45], sharp turns in photonic crystal waveguides [37], and transitions between traditional index-guided and photonic crystal waveguides [33]. These previous works, however, have relied on an initial guess of the geometry of the structure. This initial geometry is then optimized through the EA to maximize the performance of the structure. While this mechanism helps in vastly improving the performance of photonic structures, it usually does not lead to conceptually novel structures.

2.4 Design and Implementation

2.4.1 Design

We combined evolutionary and finite difference time domain algorithms to address interesting problems in photonics. Typically we simulate the propagation of pulsed or constant wavelength light through a geometry made from a high and a low index dielectric, over a fixed volume of space. Once the field comes to a steady state we evaluate some aspect of the field, such as magnitude over a region or flux through a cross section. From this evaluation we form a merit value describing the performance of a given geometry. The merit value is used by the EA to search for an optimal structure geometry. The EA algorithm was always tested with completely random initial solutions as well as solutions which start from empty, the EA converged to qualitatively equivalent solutions. We operated the FDTD around the 1550 nm wavelength range and discretized the computational grid with resolution of 20-50 nm. The computational domain was typically around 5x5 microns for two dimensional problems and 5x5x3 microns for three dimensional problems.

2.4.2 Implementation

The FDTD and EA code was implemented in Fortran 90, chosen due to existence of a code base for non parallel FDTD and ease of implementation of discrete mathematical algorithms. The existing FDTD code was rewritten with a message passing interface functions MPI to support division of computational volume along all three spatial dimensions. The number of elements of edge el-

ements in a subvolume to be communicated need to be minimized to minimize time used on communication calls between different FDTD compute nodes. A minimal node count corresponds to minimum surface area of the computational subvolume. Hence, the ability to cut global computational grid into cubes is imperative (and really messy). The need for low bandwidth communication and scalability ruled out ethernet backed networks. We utilized a 1024 node CRAY XT3 supercomputer in Pittsburgh Supercomputer Center. Each node had 2 opteron chips with 2 cores each, yielding a total of 4048 CPUs. The computer used a proprietary UNIX based operating system, with a communication subsystem to minimize communication latency between the nodes.

2.4.3 Parallelization

We took advantage of the parallel nature of the EA and FDTD to minimize the wall clock (WC) time. The common terminology for the total real world time that an algorithm runs on n CPUs is the WC time, and $n * WC$ is the CPU-hours time. Since each geometry in a solution pool of size p can use f nodes by the FDTD for evaluation, we can use up to $t = p * f$ CPUs in parallel by the EA. The communications between different notes for FDTD algorithm is 100s of times per second for sufficiently small grid element count. A delay in communication introduced by network can take the majority of the total algorithm run time. Algorithms with frequent communication in between the nodes are said to have fine-grain parallelism. The EA algorithm requires very infrequent communication between nodes, algorithms of this nature are said to have coarse grain parallelism. The parallelization schemes in the combined EA-FDTD algorithm are shown in Fig. 2.3

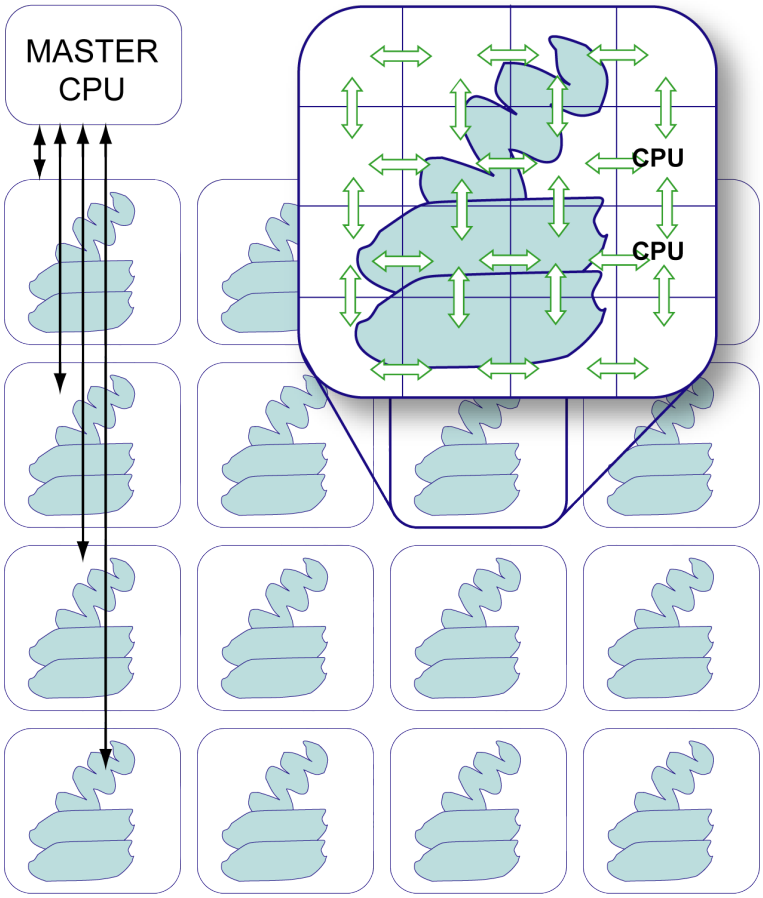

Figure 2.3: Scales of parallelism involved in combining finite difference time domain and an evolutionary algorithm. The fine grain parallelism (green arrows) in FDTD requires very low latency network. Use of fewer nodes for computing an individual geometry, increases the time in between node communication and is more forgiving of slow interconnects. Use of many nodes for each geometry decreases memory requirement per node and can significantly decrease cache missions and increase FLOPS rate.

2.5 Results

If we wish to minimize the WC time before an optimal solution is found on a system with x nodes, we can trade off solution pool size and geometry parallelization size. At one extreme we could have a solution pool size of x with no

FDTD parallelization and, at the other extreme is a solution pool of a single candidate, with highly parallel FDTD, evaluating a single geometry over x nodes. The optimal solution is somewhere in between. We must also take precautions as to avoid having some CPUs sitting idly while others are computing because no more geometries are left to evaluate.

The number of EA iterations needed to converge on a solution decreases with larger pool size. However population pools of over 1000 individuals do not significantly decrease the number of EA iterations. Once we find the optimal pool size p, we can evenly subdivide x compute nodes between all candidates to evaluate all of them simultaneously. In reality FDTD code can not practically utilize an arbitrary number of CPUs. Instead, it divides the material mesh an integral number of times along each domain. In our FDTD implementation computational domain divisions were always in powers of 2, hence $f = 2^s (s \in \mathbb{Z})$. Supercomputer centers usually operate by giving CPU-hour grants to users. The hours are used in a job queuing system, where a user requests to use some number of CPUs for arange of hours. The queuing system would favor certain sizes of allocations to maximize CPU maximization. With those constrains we could not always choose an arbitrary number of CPUs x and be able to evaluate the entire solution set at once (or we could and sit in queue for days waiting for our oddly sized allocation to come up). Hence we chose a pool size $p = f * m * n$ and $m, n \in \mathbb{Z}$, where $x = m * f$ to keep nodes from idling towards the end of the computation. Details of FDTD and EA implementation for different photonic problems will be given in later chapters in the *Implementation* sections.

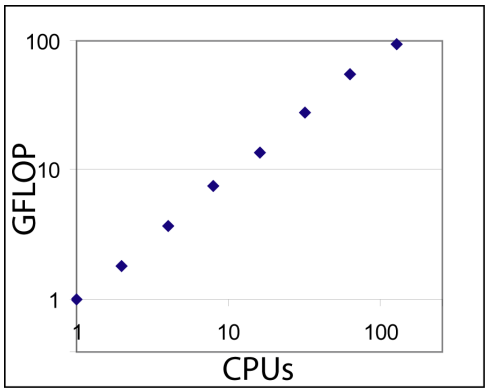

Figure 2.4: Floating point operations per second (in 10^9) with increasing number of CPUs to compute 5000 time steps on a 128x64x128 point mesh. The algorithm scales almost nearly. The increase of message passing interface (MPI) calls is compensated by less cache misses. The cache misses decrease bc fewer points are computed by each CPU, and hence more efficient use of low level cache.

2.6 Results

In evaluation of parallel algorithm performance, a common metric is the number of floating point operations per second (FLOPS). With modern CPUs, giga FLOPS, or GFLOPS is the typical of performance for an algorithm. To test the scaling of the algorithm, we ran FDTD on the same grid with an increasing number of subdivisions, and asked the system to report total GFLOPS used by the algorithm. The results are shown in Fig. 2.4.

2.7 Results

The performance degrades slowly with an increase in number of CPUs because more time is spent on communication. Overall, we see that in this parallel and efficient implementation of FDTD, WC time can be significantly reduced by two

orders of magnitude. The EA uses negligible communication resources, hence scales linearly. So to evaluate a pool of size f with 1 compute node takes f times longer than if f computers nodes were available. The combination of EA and FDTD parallelism allowed us to efficiently run FDTD code on over 4000 CPUs in parallel with 0.8 over 3.2 tera-FLOPS (TFLOPS) average performance.

2.8 Summary

Evolutionary algorithms combined with a parallel finite-difference time-domain algorithm were implemented on a large supercomputer. The algorithms showed excellent scaling while utilizing up to 4000 processors and a number of photonic problems were addressed with details in chapters to follow.

CHAPTER 3

APPLICATION: CONFINEMENT AND PERIODICITY

3.1 Introduction

Photonic structures consisting of periodic patterns of high and low index materials can alter the distribution of an electromagnetic field in space and frequency [57, 80]. Applications include light emitters, modulators, switches, etc. [72, 22, 3]. Periodic photonic structures have traditionally been hand designed with some insight from the extensive research of crystalline atomic lattice structures, where an analogy between electronic functions in crystalline structures and waves in periodic media with different dielectric functions is drawn. Based on these designs, photonic structures that confine light and enhance and inhibit its propagation in specific directions have been demonstrated [49, 27, 35, 12]. It is not clear, however, if the periodicity of photonic structures is a necessary condition for controlling the distribution of light. This question is especially relevant since on one hand, localization has been demonstrated in random media [78, 39] while on other hand, recent discoveries of periodic photonic structure in biology [8, 54] indicate that viable patterns can emerge through blind natural selection, suggesting that the periodicity of the structures is a principal condition for effective light manipulation. In order to address this question, we use an EA combined with FDTD algorithm to explore confinement of light starting from completely random structures without any innate periodicity. More specifically, we wish to explore localization in dielectric media. Highly localized fields are important for enhancing the degree of light-matter interaction [58], including nonlinearities [3] for modulators and switches. It is also important for

controlling the spontaneous emission rate [57, 13] for ultra low threshold laser applications [1].

3.2 Implementation

We represent our photonic structure as a 90 x 90 matrix with binary elements. Each element corresponds to a high or a low refractive index square region (nH and nL, respectively) of 20 x 20 nm in the material. The structure is evaluated using Finite Difference Time Domain (FDTD) simulation. In the simulations a continuous wave light (wavelength of 1.55 nm) is coupled into the structure via a waveguide (see top of Fig. 3.1(a)). The FDTD simulations are performed for light polarized with the electric field parallel to the propagation plane.

The EA uses a pool size of 180 solutions. The crossover operation swaps random rectangular subsections between the two candidate matrices. The rectangular region is chosen randomly from a toroidal mapping of the matrixes; this guarantees equal probability for all parts of the structure to be swapped. The mutation operation flips the binary value of each element in the structure with some probability. Each binary element is flipped with 0.1% probability. The result is added to the pool of new candidates.

3.3 Results

Figure 3.1 shows the evolution of our simulated structure n_H 3.5 and n_L 1.5. The dark and light regions correspond to the high and low index regions, respec-

[1] Portions of this chapter are reproduced with permission from [24, 23]

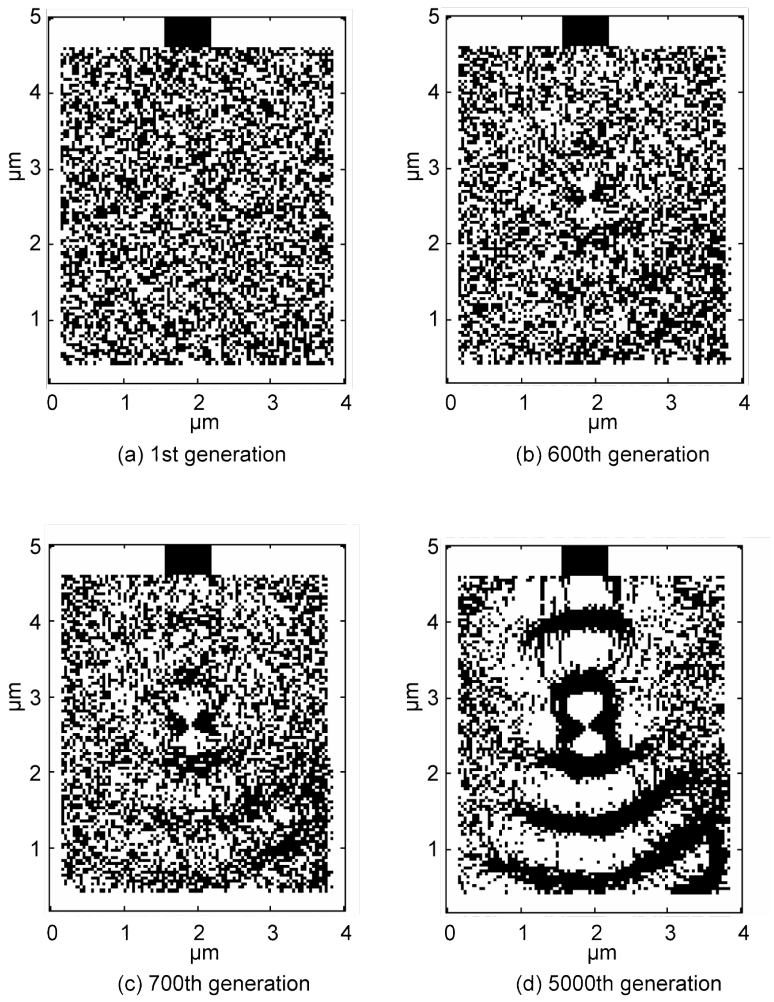

Figure 3.1: Evolution of resonator, (black: high index, white: low index. (a) Random starting solution, (b) bowtie slot begins to form, (c) distributed Bragg reflector layers begin to form, (d) the DBR and the bowtie are clearly defined

tively. Different generations of the evolution are shown. In the first generation, Fig. 3.1(a), the solution candidates are completely random. In the later stages, Figs. 3.1(b)1(d), one can clearly see well-defined structures, see Fig. 3.1(d). The EA was tested several times, each time starting from a completely randomized solution set, and each time converging to a slightly different value of the merit function, but always with qualitatively similar structure as one in Fig. 3.1(d). In Fig. 3.2 we show the same structure as in Fig. 3.1(d) with 40 nm grid size,

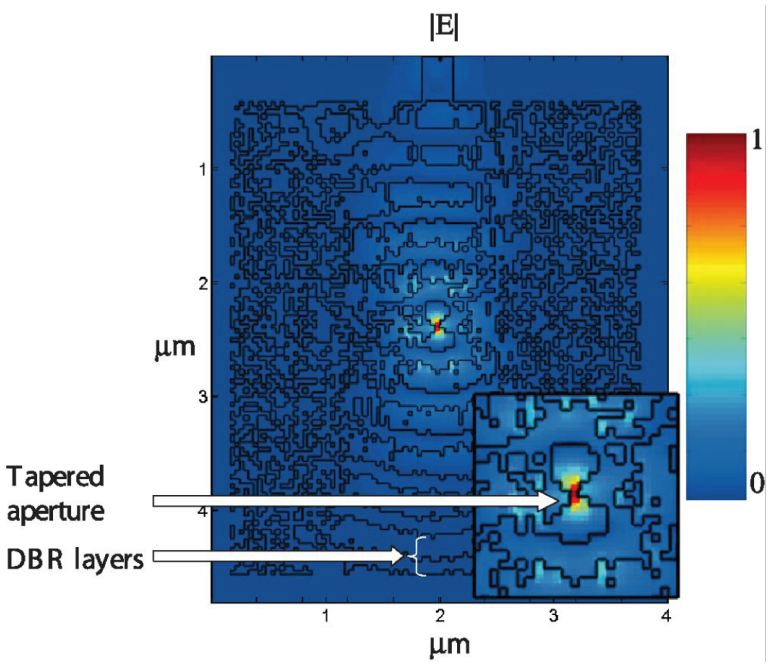

Figure 3.2: Normalized field amplitude of optical mode in an evolved resonator (5000th generation). The inset shows magnified view of the structure center where most of the field is localized

together with the spatial field distribution. In Fig. 3.1, one sees a strong enhancement of the electric field at the center of the structure, approximately 40 times of the amplitude of the incident light. The inset shows that most of the field is localized in the center of the structure with a small modal volume. The effective modal volume [13] is estimated to be $0.112(\lambda/2n)$. The quality factor Q of the structure is 300. Q was calculated from the simulated excitation spectrum of the cavity. One can see in the evolved structure, shown in Fig. 3.1(d) and 3.2, periodic alternating layers which spontaneously emerged from the simulation. The structure consists of alternating high and low index regions resembling distributed Bragg reflectors [61] (DBRs) with a small aperture in the center. The periodic alternating layers have a periodicity approximately equal to $\lambda/2n_{material}$, and are responsible for the relatively high Q of the structure.

3.4 Results

The small aperture in the center of the structure with a bowtie geometry leads to the high confinement and ultrasmall modal volume. The effect of this geometry can be understood by noting that the phenomenon of strong light localization in a narrow low index region was recently demonstrated using slotted waveguides [79]. This phenomenon occurs due to the strong field discontinuities at the boundaries between two high index contrast regions. In Fig. 3 we show the field amplitude distribution ($|E|$) for a field polarized in the direction parallel to the propagation plane. In the evolved structure, the bowtie geometry consists of a slot region formed by two high index tapers. These tapers localize the field in the vicinity of the slot leading to light localization in the direction tangent to the interface, Fig. 3.3(b), as well as normal to it, Fig. 3.3(a), as shown in solid lines. This 2D localization yields a stronger degree of confinement of the mode compared to a straight slot due to its 2D nature. The strong light localization nature of the structure in the slot region leads to the ultra small modal volume of,

$$V_{eff} = \frac{\int \epsilon(r)E(r)E^*(r)d^3r}{\epsilon\left(r_{\max}\right)\max\left(E(r)E^*(r)\right)} = 0.112\left(\frac{\lambda}{2n}\right)^3. \tag{3.1}$$

The strong field discontinuities mechanism is responsible for this higher localization and therefore leads to a modal volume that is almost an order of magnitude smaller than the ones achieved with photonic crystal resonators [65, 79] that are enabled by the wavelength dependent reflectivity of the crystal surrounding the cavity. We compare the performance of the EA to the performance of a baseline random search. Figure 3.3 demonstrates the relative light intensity in the slot with successive generation of search algorithms. Error bars are derived from different randomized initial conditions. The evolutionary algorithm

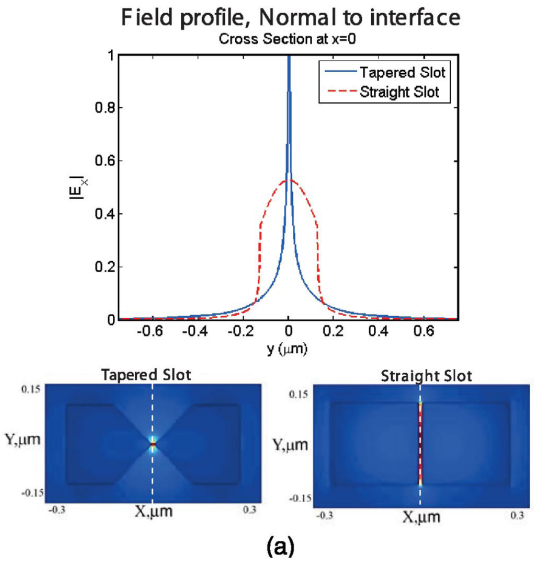

Figure 3.3: Propagation through voided structures. (a) Field localization, normal to the interface. (b) Field localization, tangent to the interface.

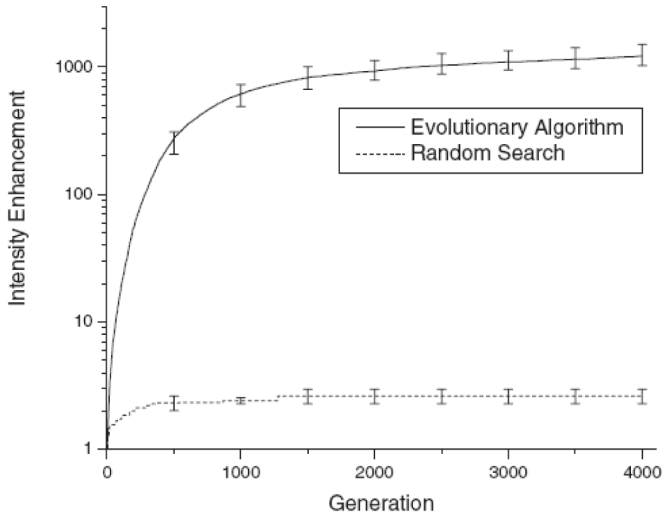

Figure 3.4: Convergence of evolutionary algorithm and a random search. The random search converges at a local minimum

results in the enhancement of intensity by almost 3 orders of magnitude relative to input intensity. We plot the merit function over 4000 generations in Fig. 3.4 for a typical run. We used a local cluster of 30 computers to evaluate a total of 288,108 evaluations in 17 hours.

3.5 Summary

In summary, we simulate an evolutionary process in the lab for designing novel photonic structures, which has resulted in a periodic structure. The structure shows a high field enhancement in the center due to emerged periodic reflectors and a novel structure with bowtie geometry that confines light in an ultra small modal volume. The emergence of the periodicity suggests that periodicity is a principal condition for strong light manipulation.

CHAPTER 4

MINIMIZATION OF MODAL VOLUME

As described in a previous chapter photonic electromagnetic structures, specifically resonant cavities are a critical element for optical devices such as lasers, filters, and switches. The cavities are characterized by modal volume, V and quality factor, Q. High Q and small V are important in increasing light-matter interactions in processes such as spontaneous emission, nonlinear optical processes, and strong coupling. The control of these interactions is essential in low-threshold nanolasers [53], quantum information processing devices [50], and photonic chips. Small volume plasmonic cavities have been suggested [47, 19], however, the presence of the metal increases fundamental absorption and limits the Q values. Dielectric structures with high Q and small V have been demonstrated, most with diffraction limited modal volumes [2, 9, 73, 70, 71] or low Qs [58].

In the previous chapter we demonstrated a light confining geometry simulated in two dimensions. In that type of simulation the third dimension is extended to infinity and final solution is a combination of infinitely extended plane waves. Here, we propose a resonator with single dielectric layer geometry of subwavelength thickness with an ultra-small modal volume. The challenge of low modal volume of dielectric cavities lies in the facts that as the modal volume of the light in the cavity approaches the diffraction limit, the diffraction losses near the reflector region increase and consequently decrease the Q and decentralize the optical mode. In a homogenous dielectric medium a propagating plane wave is diffraction limited in its width to $\sim \lambda/2n$, where n is the refractive index of the dielectric. Micro photonic devices are typically limited

to dielectric materials with indices up to n=3.45 (Si). A cavity with two perfect mirrors spaced half wavelength apart thus has a resonant mode volume of no less than $\sim \lambda/2n$. Low modal volume holey waveguide (HW) cavities have been shown before [58], consisting of 2 dielectric Bragg mirrors inside of a Si waveguide, the modal volume was achieved as low as $\sim 5.8(\lambda/2n)^3$.

4.1 Implementation

The cavity proposed here with modal volume of $0.01(\lambda/2n)^3$ and $Q = 10^3$ is based on a structure found with an EA. Figure 4.1 is a schematic of a planar dielectric cavity designed with an evolutionary algorithm (EA). We represent the shape of a resonator as a 100x100 matrix of binary elements, corresponding to high and low index dielectric in the slab. The high index material has a thickness of 250 nm. The size of the computation domain is 4.8x4.8x3.0 microns. The merit function for a low modal volume cavity is the value of the field amplitude in the center of the optical mode, as in the previous chapter. The cavity is excited via a normally coupled waveguide (top of Fig. 4.1a-d). The excitation is simulated using FDTD algorithm in 3D. The EA ran on 2000 Opteron CPUs for 12 hours to arrive at the solution shown in Fig. 4.1d.

4.2 Results

The evolved cavity, Fig. 4.1d, resembles a bowtie, Fig. 4.2, embedded inside of a 1-D photonic crystal waveguide. The cavity achieves an ultra-low modal volume with a slot region shortened to a point in the middle of the bow-tie.

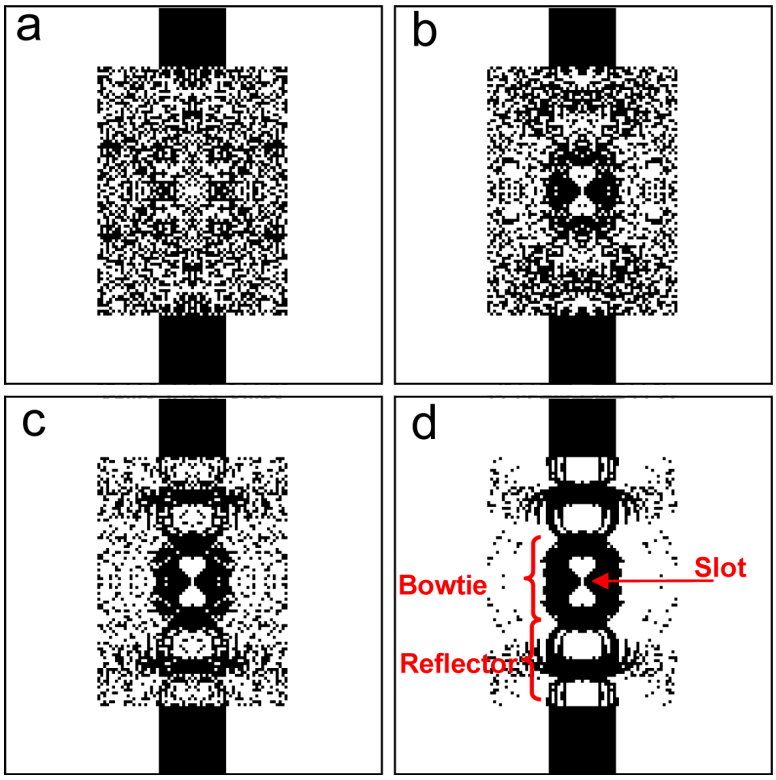

Figure 4.1: Evolution of a planar resonator in an evolutionary algorithm; a) 1st generation, completely random device; b) 100th generation, the bowtie shape is defined, c) 200th generation, the bowtie shape is well defined and grating like structure begins to emerge; d) 800th generation, the bowtie and the grating like structure are cleanly defined; each image is 120x120 pixels, each pixel represents 40x40nm square peg 250nm high in a 3D finite difference time domain simulation. The simulation domain of FDTD is 4.8x4.8x3.0 microns

In contrast to the disk, ring, and photonic crystal cavities, the electric field is localized in the low index material. The geometry found utilizes electric field discontinuities to decrease the modal volume of the cavity below $1(\lambda/2n)^3$. Displacement field normal to a dielectric interface must be continuous to satisfy the boundary conditions; consequently the electric field normal to an interface is discontinuous. The discontinuity leads to a field maximum in the low index dielectric[13, 14]. This effect can be utilized in a narrow low index dielectric slot

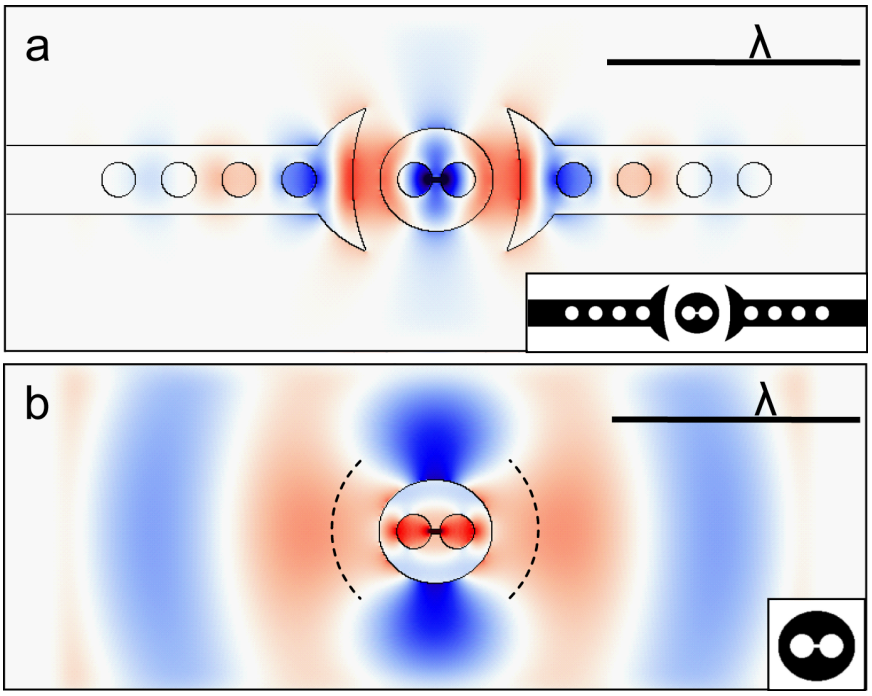

Figure 4.2: a) Resonant mode amplitude (E) in a planar bowtie cavity; b) radiative mode amplitude (E) in a bowtie, the dotted line represents the curvature of radiating field; insets, dielectric geometry of the respective devices, white: low index oxide 1.45, black: high index silicon 3.45

placed in a high index dielectric waveguide. The modal cross section area of a single mode silicon waveguide with a 40 nm air slot is $\sim 0.02(\lambda/2)^2$, significantly lower than the diffraction limit. A slot waveguide resonant cavity with Bragg mirrors have been measured to have Q of 300 and a calculated modal volume $\sim 0.04(\lambda/2n)$[58]. The bowtie center found with EA in Fig. 4.2a, has a strong electric field (Ey) enhancement in the center of the cavity mode due to the slot effect similarly to Fig. 4.1d.

The proposed cavity shown in the inset of Figure 4.2a, is inspired by the evolved structure (Fig. 4.1). The center of the cavity is a bowtie shape to provide discontinuity effect localization. The outer ellipsoid of the bowtie is shaped to

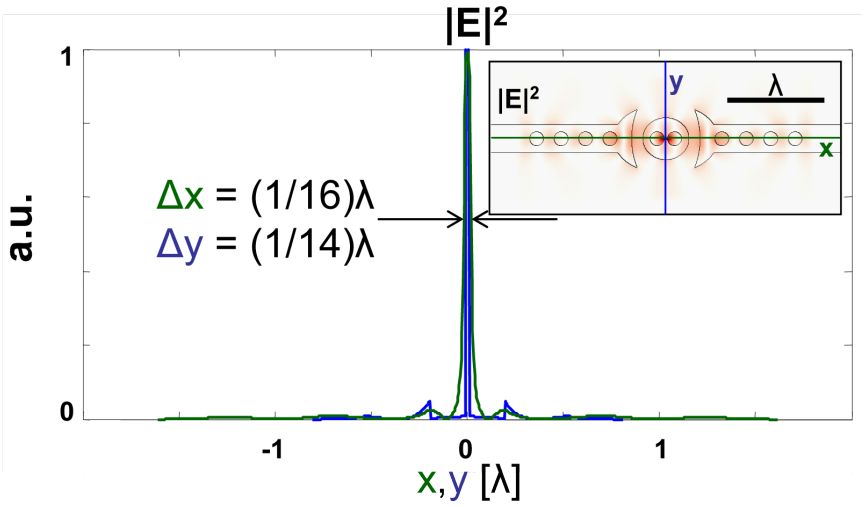

Figure 4.3: Mode intensity in the bowtie cavity: blue, along the length and green in the transverse direction. The inset shows intensity distribution of a resonant mode in a bowtie cavity. Note the peak width is below a tenth of a wavelength in both dimensions.

minimize emission into the y direction. Figure 4.2b shows the field distribution of the isolated bowtie. One can see that the bowtie emits a dipole-like radiation and is not a resonant cavity, hence a reasonable Q can not be realized. We address these losses by embedding the bowtie in a cavity with curvature of innermost surfaces matching the centermost nodes of the field radiating from the bowtie shown in Fig. 4.2b (dotted line). The radiative mode from the bow-tie is therefore contained by the surrounding Bragg mirrors with a wide bandgap (100nm) matching the radiative wavelength. The coupling to the waveguides and the Q of the cavity can be controlled by the number of holes in the waveguides. The field intensity of the resonant mode is plotted longitudinally and transversely to the center of the cavity in Fig. 4.3. We note that in both dimensions the field peak is confined below the half wavelength of the light and approaches a delta function.

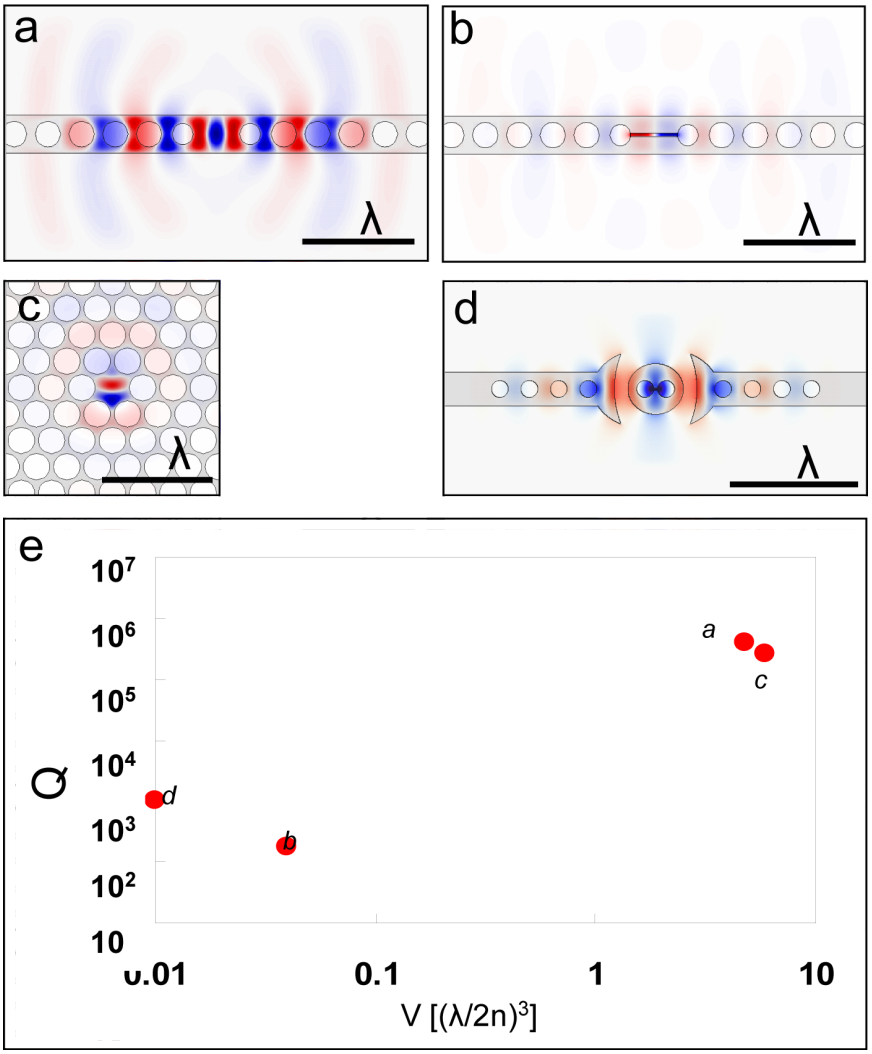

Figure 4.4: Resonant modes in various planar cavities; e) Q vs V values of the above cavities; a) holey waveguide; b) holey waveguide with slot, field localized in low index medium; c) photonic crystal defect; d) bowtie cavity, field localized in low index medium;

4.3 Summary

High confinement planar cavities have been proposed in various configurations, Fig. 4.4g. Ring cavities confine light within a waveguide and fundamentally only suffer bending losses. The radius of a ring cavity can be increased to in-

crease Q's while increasing waveguide length and modal volume. The modal volume in ring cavities is at least two orders of magnitude above the half wavelength diffraction limit, Figure 4.4a. Ring cavities with an off center slot can have significantly lower modal volumes than ring cavities while maintaining high Q values, Fig. 4.4b. Planar 2D photonic crystal defect cavities [2, 70, 71, 41, 46] have been proposed with Q's as high as 10^6 and modal volumes just above the diffraction limit $< 10(\lambda/2n)^3$. A schematic of an example cavity is in Fig. 4.4, optimized cavities tend to have perturbed hole sizes and spacings near the defect. Holey waveguide cavities [73] have comparable modal volumes and Qs to 2D PCD cavities. Introducing a slot in the waveguide of HWC [58] reduces the modal volume below the diffraction limit to $0.04(\lambda/2n)^3$ and Q to ~300. The proposed planar bowtie cavity has a modal volume of $0.01(\lambda/2n)^3$, smaller than any reported dielectric resonator and has Q of 1000. The high Q is achieved by suppressing radiation from a dipole mode in a bowtie geometry. The dipole like mode in a bowtie is coupled to a one dimensional photonic crystal waveguide. Our design not only achieves a record small volume but also confines the peak field to the low index material, which can maximize light-matter interaction with gasses and liquids.

CHAPTER 5

APPLICATION: MODE CONVERSION

5.1 Introduction

In order to minimize light loss in integrated devices, they must efficiently convert guided modes between different photonic components. We consider cases of internal and external guided modes, such as light from an external source coupling into an integrated waveguide. Also we consider coupling of identical modes with opposite propagation directions. In both of those problems known periodic geometries exist, and exhibit various degrees of performance. We will explore the necessity of periodicity and aperiodicity in the two mode conversion schemes.

5.1.1 Grating Couplers

In many cases light must be coupled out of an integrated device for processing and measurement. Glass fibers are the standard carriers of coherent light in telecommunications. Efficient and simple coupling of light between an integrated package and an optical fiber is necessary for the study and commercialization of photonics. This area of the field is still in continuous development and is one of the barriers, if not the largest barrier from the wide spread commercial application.

Common optical fiber (SMF28) has a 9 micron core and supports only a single guided mode in the telecommunication band. The mode field diame-

ter (MFD) in this fiber is ~13 microns. A single mode integrated waveguide made from silicon as the high index material and silicon dioxide as the low index cladding, has a significantly smaller MFD, below 0.5 microns. The vast mode mismatch between the two waveguides leads to coupling losses above 10 dB. Two practical approaches currently exist to efficiently couple light between integrated waveguides and fibers: inverse tapers and gratings.

An inverse taper is an adiabatically narrowed waveguide terminating at the edge of a chip [4]. A sufficiently narrow waveguide will have a strongly delocalized mode and hence a MFD to closely match one of a fiber. The photonic chip must be cut across the end of the taper and polished to minimize scattering losses. Inverse tapers have no fundamental losses, and experimental losses have been shown under 3 dB per facet [43].

The later approach is to taper out a waveguide and terminate it with a surface grating, which will support an upward radiating mode. This approach eliminates need for cleaving and polishing the die [5, 42, 68, 69, 75, 76, 77]. Grating couplers can be placed anywhere on the die surface and do not require post fabrication polishing. They allow for a simplified arrangement of photonic devices on a chip and can easily accommodate coupling to cleaved fibers with arbitrary MFD. On the downside, gratings exhibit very strong polarization and wavelength dependence. They typically require extra fabrication steps to maximize coupling efficiency. Since most of the light leaving a fiber coupling to the grating will pass through it, reflective layers underneath the grating are usually used. The layers reflect light towards the grating and give light another chance to couple into the waveguide. Without auxiliary reflective layers, insertion loss is typically 10 dB/facet. A single reflective metal layer can be used to return the

transmitted light to a grating, or multiple dielectric layers are stacked to create a distributed Bragg reflector. With and without assistance of reflection, grating coupling schemes suffer from back reflection into the waveguide. In certain applications back reflections are highly undesirable, as they can destabilize a source laser or interfere with a duplex data stream.

We utilized an evolutionary algorithm to design an aperiodic grating to minimize back reflection and maximizing coupling efficiency from the fiber to the integrated waveguide.

5.1.2 Reflector

For integrated photonics to be a versatile platform to develop devices and systems, analogs of basic free space optics elements must be efficiently implemented. Metal mirrors, common and simple elements do not directly translate to integrated photonic devices, where metals are usually avoided to simplify the fabrication and reduce losses. In fiber optics it is typical to 'write' a grating into the fiber by altering index of refraction via intense UV light. Integrated waveguides with periodic index modulation, or periodic width modulation have been shown to act as reflective gratings but usually have high insertion losses.

A 'mirror' design has been show and widely implemented in high confinement waveguides by introducing a defect in the photonic band gap structure [18]. A periodic array of holes in a waveguide create a bandgap with a limited number of allowable guiding modes. Light traveling in an unperturbed waveguide is coupled to a backward propagation mode when it encounters a bandgap periodic region due to a lack of allowed propagation modes. We wanted to see

if the EA could rediscover such periodic reflecting structures starting from an arbitrary geometry.

5.2 Implementation

5.2.1 Grating Couplers

We implement the reflection minimization problem in two dimensions. We use silicon nitride, a dielectric, as the guiding layer (800 nm thick), air cladding, and silicon oxide, a dielectric, as the substrate layer. The indexes of silicon nitride, and silicon oxide are 2.0 and 1.45 respectively. The output mode of the fiber is assumed to be 12 microns. We test several coupling angles, with fiber normal to the grating and tilted at 30 degrees. Our computational domain is 25x5 microns. The grid step size is 40 nm. We restricted the minimum feature size to 360 nm to match the capability of UV lithography. The trench etch depth was fixed at half the depth of the nitride layer. We optimized at wavelength of 1550 nm and 850 nm. We also performed an optimization without restriction on either the resolution or the etch depth of each 'tooth'. We used an EA with a population size of 120. Since the simulation was in two dimensions, only one compute node was sufficient to calculate each mesh in a timely manner.

5.2.2 Reflector

We setup a 500 nm wide waveguide with a forward propagating pulse emitted in the waveguide cross section, t, Fig. 5.1. We assume a flux region, r, where

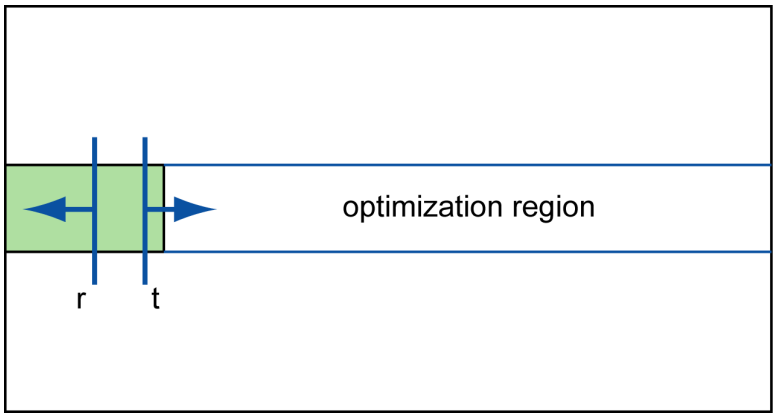

Figure 5.1: Optimization scheme for integrated reflector. On the left is a waveguide with excitation flux t pointing towards reflector. The simulation launches a pulse and monitors the reflection flux r. The merit is assigned as highest r/t calculated over spectral width of the pulse. The algorithm is limited to modifying the dielectric in *optimization region*. The high index dielectric (shaded) is 2.0, and the low index dielectric is 1.0

back propagating light is measured. The algorithm was restricted to 4x0.5 micron region in front of the waveguide. Without losing generality we forced mirror symmetry in the material region to match the excitation mode. We initialized the 'waveguide' region with random points as well as all low and high index block. The grid size over the entire domain was 20 nm. High index was set to 2 and low index was 1. Excitation pulse was polarized in the plane of propagation. We set the pool size to 120, and ran the algorithm on 49 CPUs. The two dimensional nature of the problem and relatively short evaluation time did not necessitate significant computational resources.

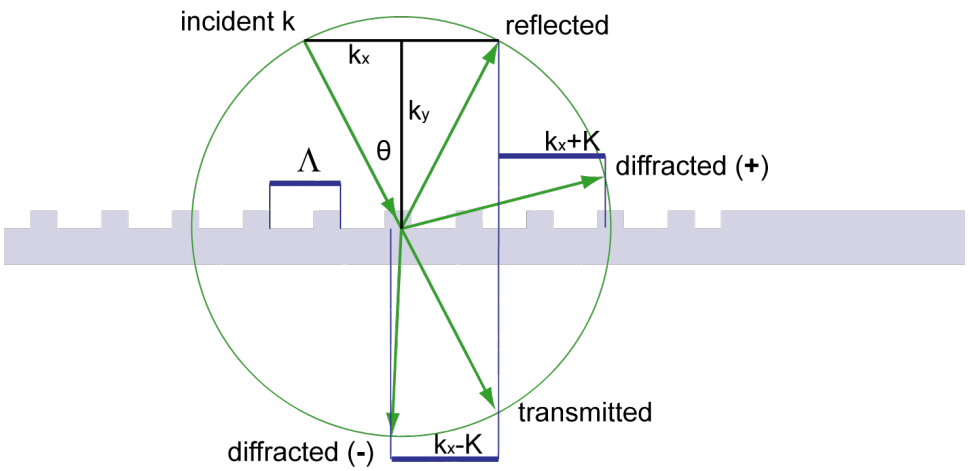

Figure 5.2: Light passing through a grating. The $\hat{x}$ vector component of the diffracted beam is altered by addition or subtraction of an integrated number of grating wave numbers $2\pi/\Lambda$. The magnitude of diffracted wave vector remains unchanged, $|k_{out}| = |k_{in}|$

5.3 Results

We first consider a traditionally designed grating coupler [55]. In Fig. 5.2 we observe the incident, diffracted and transmitted beams in a grating. The grating alters the component of the diffracted wavevector parallel to it. Hence, for grating in $\hat{z}$ the diffracted beam becomes,

$$k_{out} = k_{in} + m \cdot \frac{2\pi}{\Lambda}\hat{z}, m \in \mathbb{Z} \tag{5.1}$$

subject to the condition $|k_{out}| = |k_{in}|$. This precipitates into a trigonometric expression for the vacuum wavelength λ with a cladding index n_0,

$$\theta = \sin^{-1}(\frac{n_{eff} - \lambda/\Lambda}{n_0}), \tag{5.2}$$

where n_{eff} is the effective index of the waveguide sans grating.

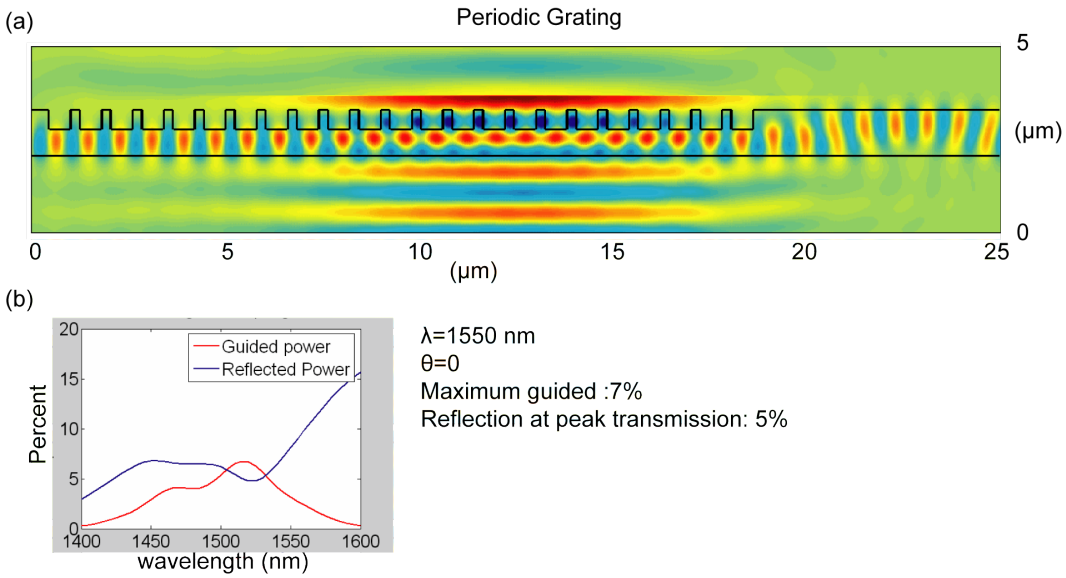

Figure 5.3: Periodic grating for coupling 1550 nm light with 0 degree incidence angle.

5.3.1 1550nm gratings

In figures 5.3,5.4 we show the periodic gratings with optimized etch depth and a duty cycle for Λ computed with Eq. 5.2, and 1550 nm incident light. In Figs. 5.5,5.6 we show evolved aperiodic gratings with the same design criteria as the periodic gratings. Note the reflected power is always 1%. We initially set the merit function for the EA as the ratio between the coupled and the reflected light. The algorithm always minimizes the reflected power to an a small value, making coupled power irrelevant. We forced the computed reflected power to be $max(1\%, Reflected)$, forcing the algorithm to stop minimizing reflected power once it drops below 1%. We justify the change to the merit function be cause the extra scattering from the surface roughness of the grating in a real device will prevent reflected power from ever reaching 0.

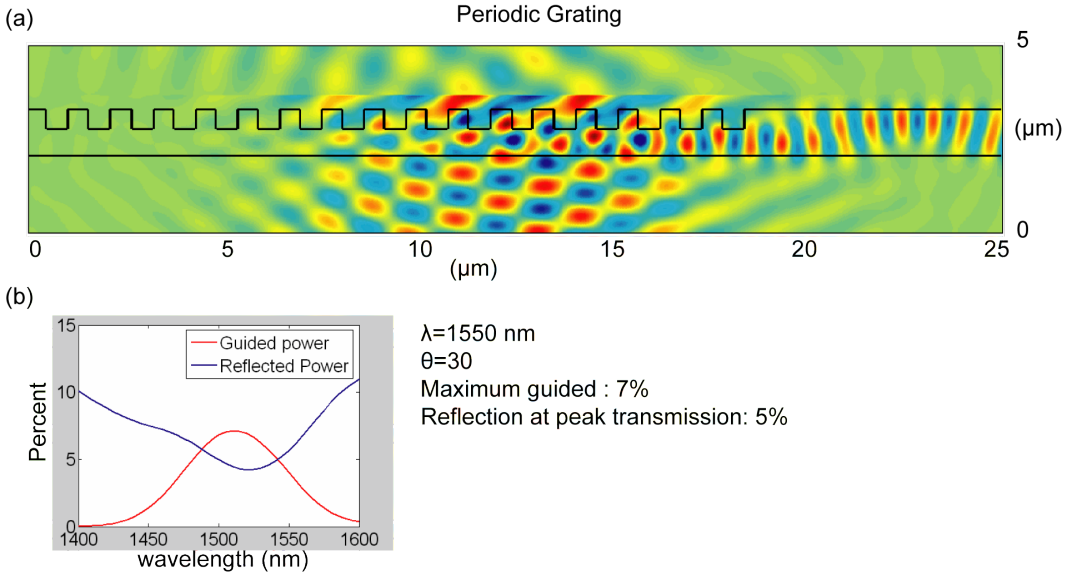

Figure 5.4: Periodic grating for coupling 1550 nm light with 30 degree incidence angle.

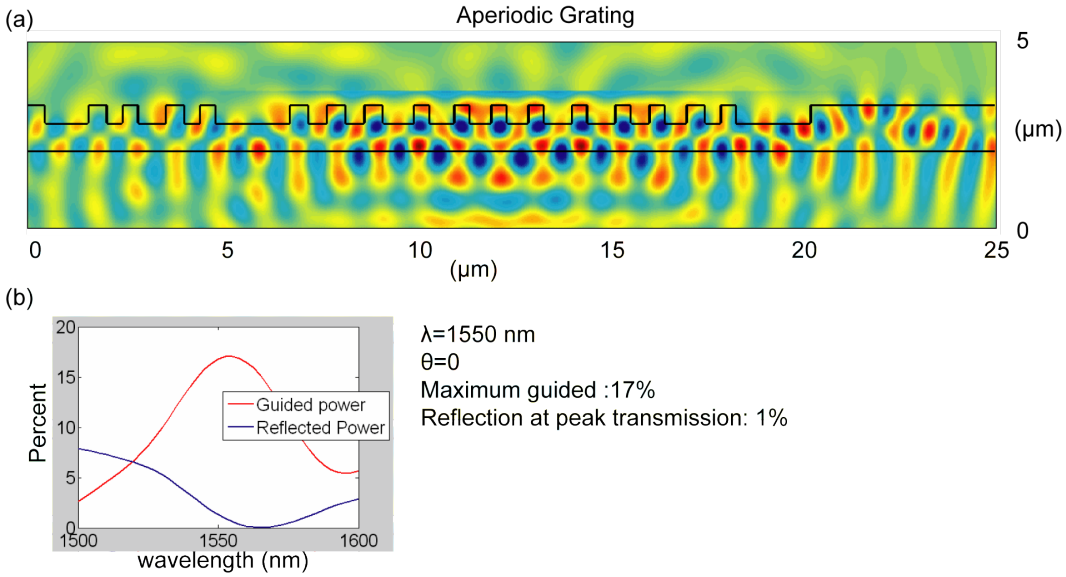

Figure 5.5: Aperiodic grating for coupling 1550 nm light with 0 degree incidence angle.

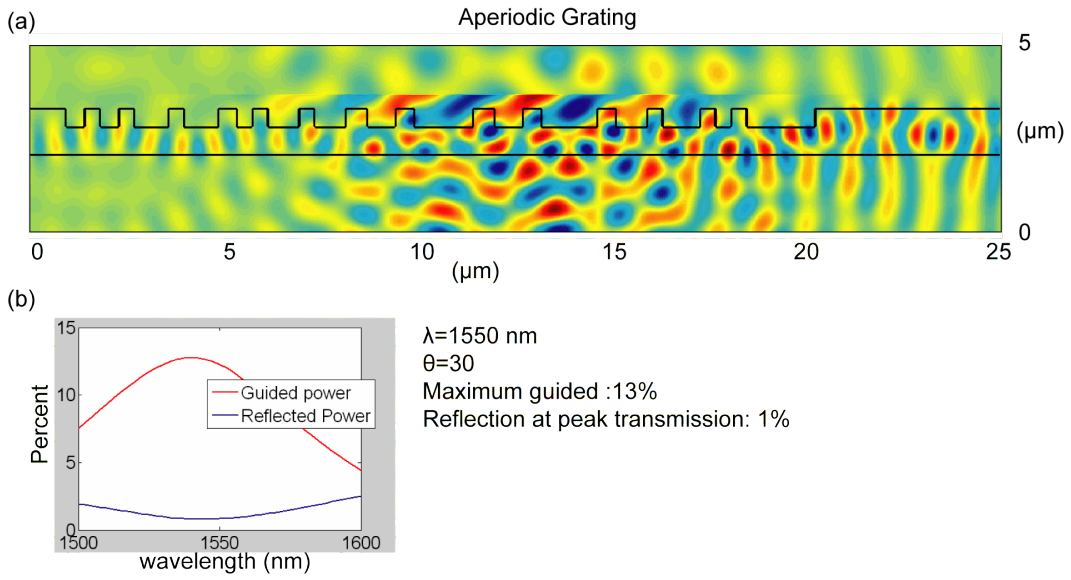

Figure 5.6: Aperiodic grating for coupling 1550 nm light with 30 degree incidence angle.

5.3.2 850nm gratings

In Figs. 5.7,5.8 we plot aperiodic grating results for 850 nm light with 0 and 30 degree incidence angles. The results for the periodic gratings are not plotted. For the periodic grating with the 0 degree incidence angle, the maximum coupling power was 4% and the reflected power was 2%. For the 30 degree incidence angle, the periodic grating had 10% coupling and 3% reflected power. Again, the EA outperforms the periodic design. The performance of periodic grating with normal incidence is particularly poor compared to other periodic designs. This can be attributed to a short grating period of ~480 nm and a high aspect ratio of the etched features. For the 30 degree angled incident light the periodic grating performed noticeable better than for the normal incidence be cause of longer ~650 nm grating period. The aperiodic grating was at a particular disadvantage since the algorithm did not allow it create features below 360 nm, a requirement was not enforced on the periodic grating.

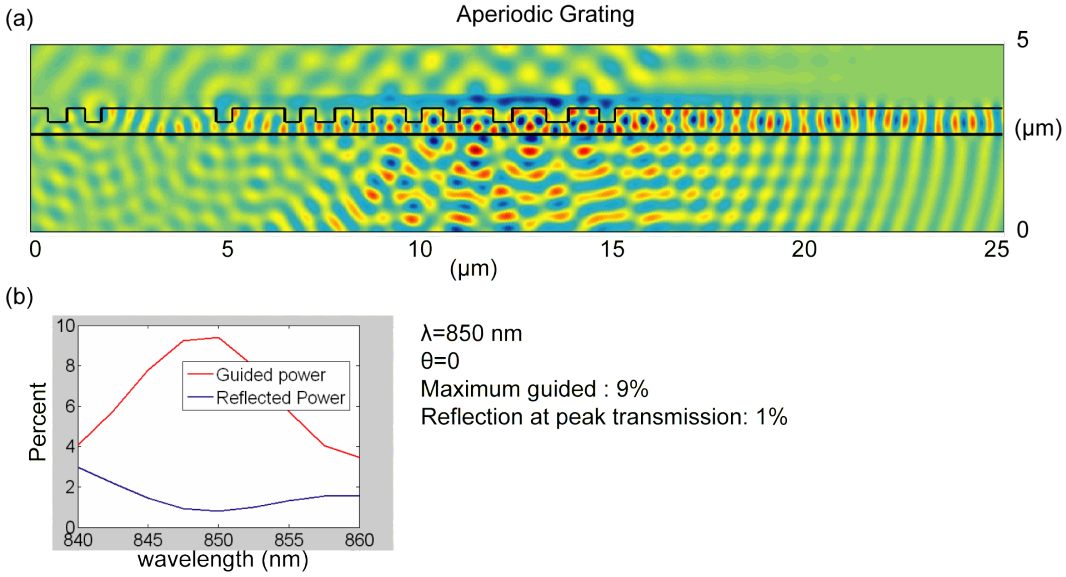

Figure 5.7: Aperiodic grating for coupling 850 nm light with 0 degree incidence angle.

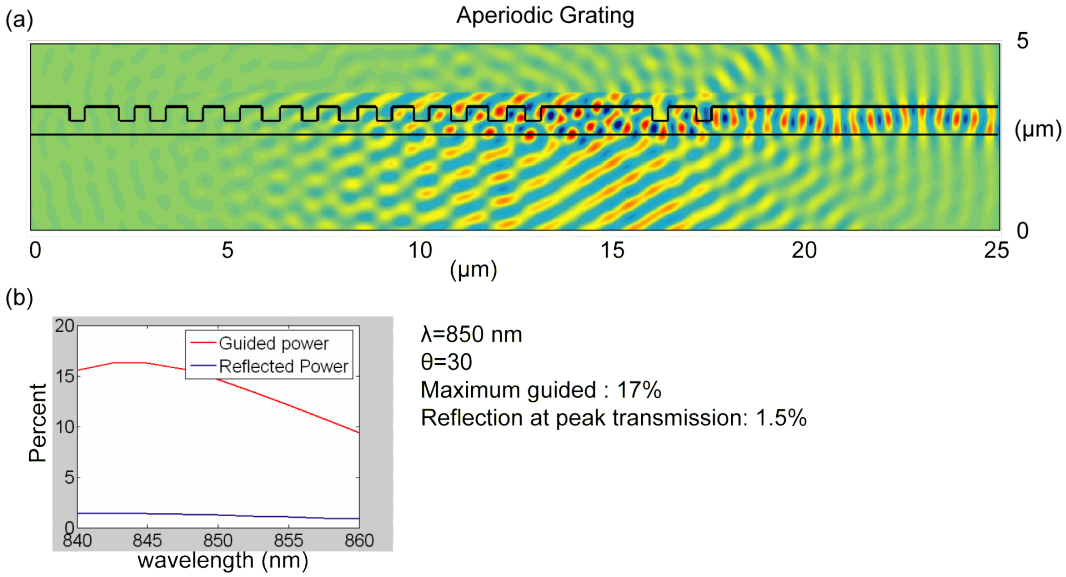

Figure 5.8: Aperiodic grating for coupling 850 nm light with 30 degree incidence angle.

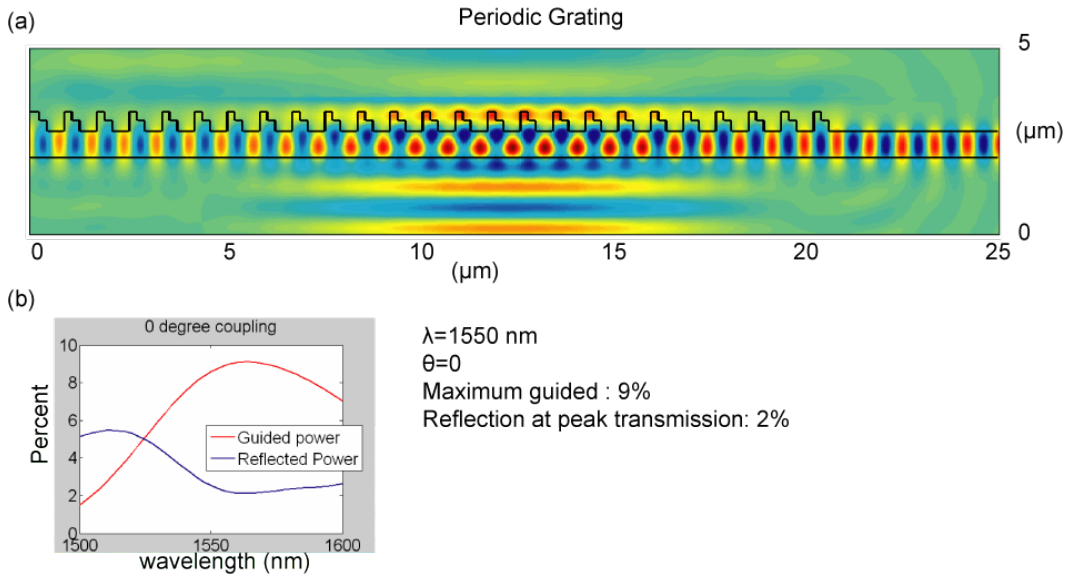

Figure 5.9: Periodic grating for coupling 1550 nm light with a 0 degree angle. Grating designed with a 2 step etch to minimize reflected light.

5.3.3 Unrestricted optimization

We present results from an unrestricted optimization in Fig. 5.10, with different guide layer thicknesses. They show exceptionally high coupling power. We observe that each solution consists of a central grating with angled ridges, and another grating with a shortened period on the opposite side from the guided direction. The period in the secondary grating forms a bandgap, and reflects light guided in the waveguide back. If we consider methodology of Fig. 5.2, the secondary grating has a wave vector $\frac{2\pi}{\Lambda}$, equal to twice the wavevector of the unperturbed waveguide guided mode. Upon encountering the grating, the final wavevector is $\frac{2\pi}{\Lambda} + \frac{2\pi}{\lambda} = -\frac{2\pi}{\lambda}$, a simple reflection backwards. The angled center grating uses the break the ridge symmetry to preferentially couple light in one waveguide direction over another. The angled surface also prevents back reflections into the fiber.

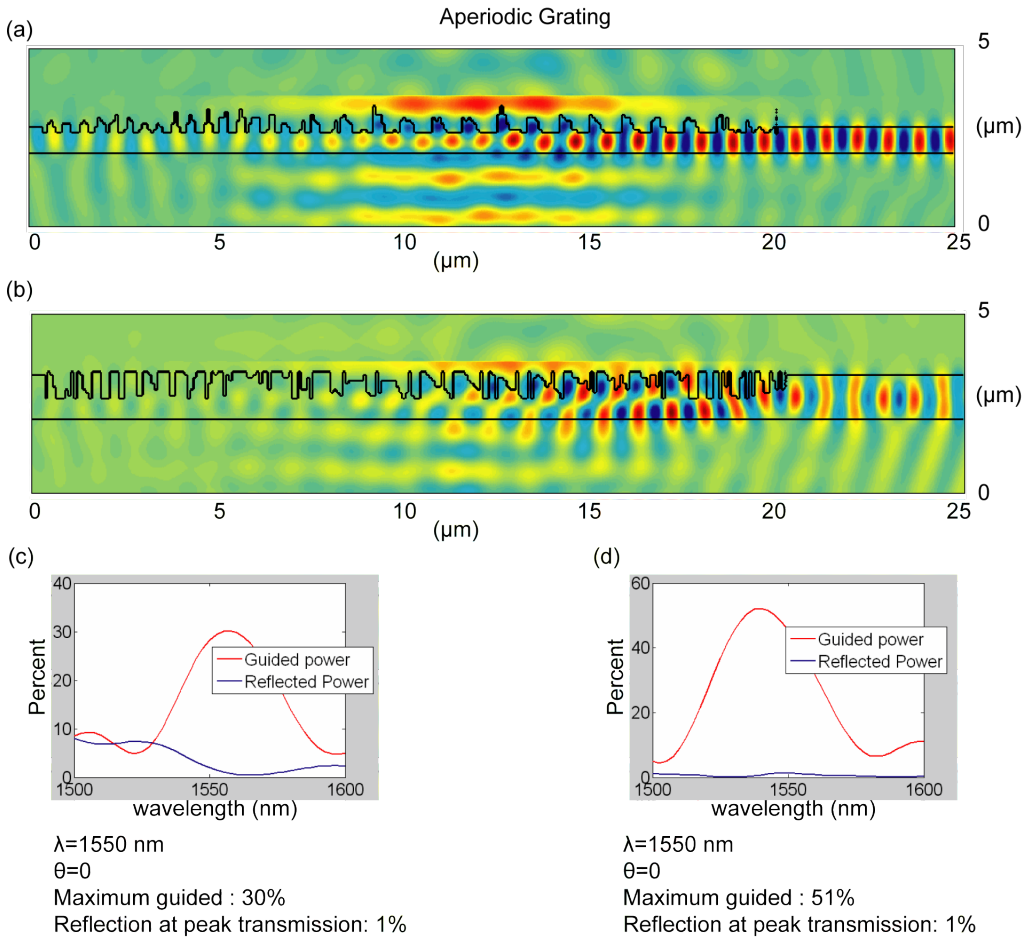

Figure 5.10: Aperiodic grating for coupling 1550 nm light with 0 degree incidence angle. The algorithm was not restricted to depth of etch or minimum feature size; (a),(c) results for material thickness of 600 nm; (b),(d) results for 1200 nm material thickness

Similar designs have been previously proposed to optimized coupling power into waveguides by using grayscale lithography [6]. We attempted to design a dual depth level grating by hand, for a similar effect of the one optimized by EA. The periodic 'blazed' grating in Fig. 5.9 did not have significantly improved performance over a single depth etch grating.

5.3.4 Alignment tolerance

In the packaging process, the coupling fiber must be fixed to the grating by epoxy or other means. Active alignment can be used, where coupling fiber is guiding light while moving. The coupled light could be monitored during alignment to find the optimal fiber position. However, during epoxy curing, or other means of fixation some misalignment is still introduced. We measured the offset tolerance for the aperiodic grading, 5.11. A misalignment of ±3 microns is possible while still maintaining better performance than the periodic grating.

5.3.5 Bandwidth optimization

In the previous optimization we looked at transmission at a single wavelength. In Fig. 5.12 there is a ~10 nm misalignment between the peak transmission and the minimum reflection wavelengths for the infrared light coupled at a 30 degree angle into a high resolution grating. We reran the EA with the merit function averaged over a 20 nm range. The transmission curves in Fig. 5.12 did not change their shape significantly from the peak wavelength optimization, but had a much better peak/minimum overlap, ¡1nm.

5.3.6 Reflector

The algorithm consistently converged at a periodic holey waveguide structure, Fig. 5.13. The field amplitude reflectivity was over 98% in all cases. We note a variation in hole size and a set of notches on waveguide edge outside the

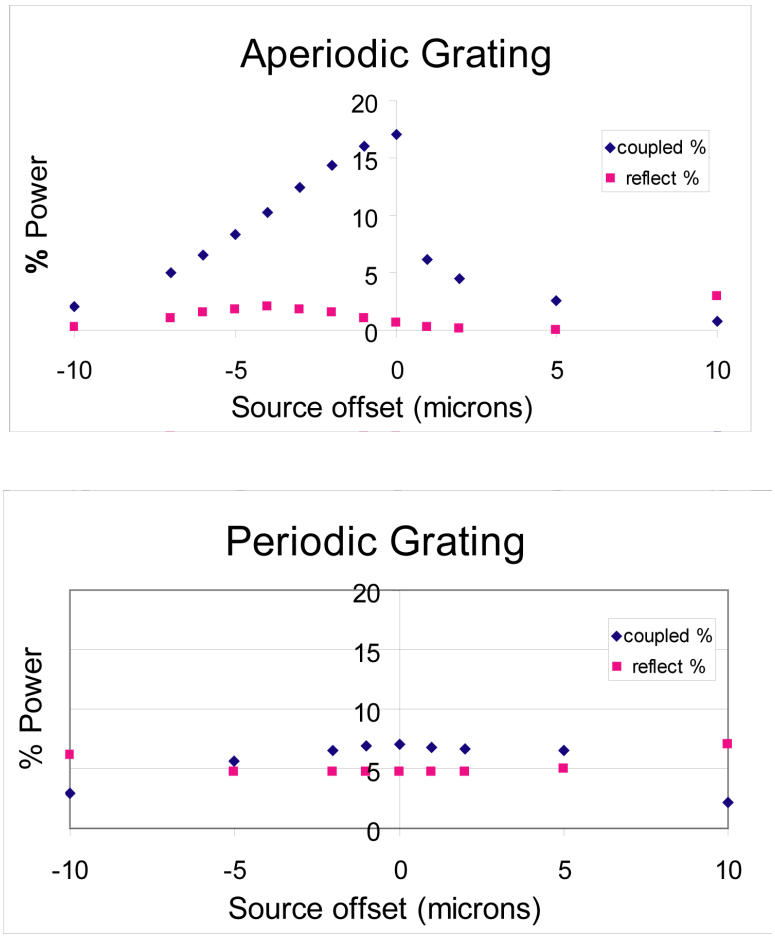

Figure 5.11: Change in transmission due to fiber offset error over the grating.

holes. These features seem to increase the reflectivity over a manually designed holey waveguide with constant hole sizes. The hand designed structures never exceeded over 95% amplitude reflection. Coincidentally over the past several years a number of papers have been published on tweaking hole positions and radii in 1D and 2D crystals with defect cavities. While radii perturbation is a common approach in increasing confinement, introduction of notches is yet to appear.

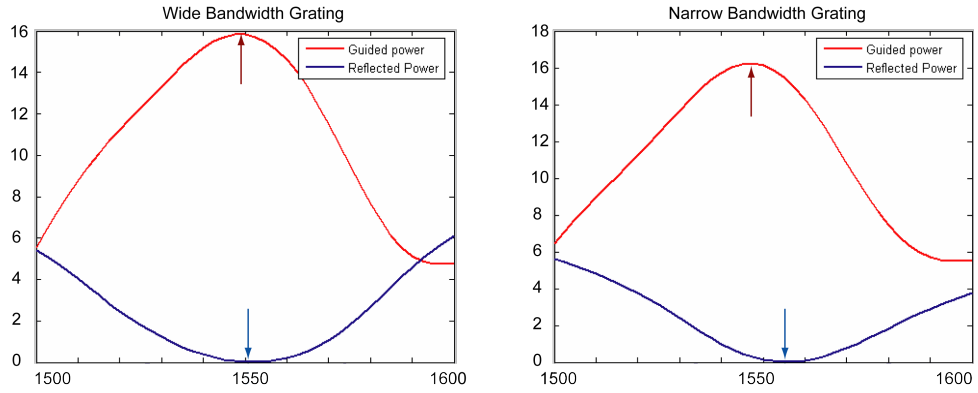

Figure 5.12: (a) Grating optimized for transmission over a 20nm range, the peak transmission and minimum reflection are spectrally aligned; (b) Grating optimized for peak transmission at a single wavelength, the reflection minimum is offset from transmission at peak, giving slightly higher transmission at center wavelength.

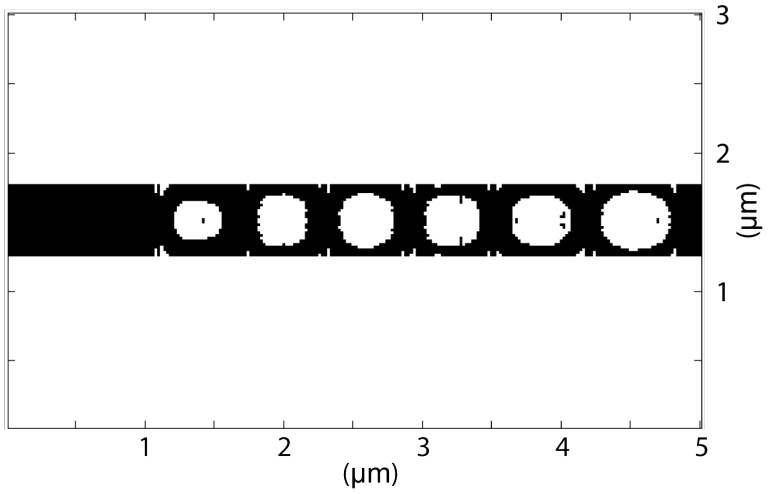

Figure 5.13: Optimized integrated reflector. The peak amplitude reflection is 97%, waveguide width is 500nm. Algorithm started from random dielectric distribution. The unevenly spaced holes, unequal radii appear to increase coupling efficiency over translationally symmetric reflector. The high index dielectric (shaded) is 2.0, and the low index dielectric is 1.0

5.4 Summary

We demonstrated a fundamentally different design approach for propagation mode transformation structures. Periodic gratings, showed a factor of ~2 increase in the coupling efficiency, and a complete lack of reflection within practical experimental limitations. The aperiodic gratings outperformed traditional designs even if sufficient resolution was not available for a correct grating period and duty cycle. We showed the versatility of the EA for design to compensate for alignment errors in the device packaging. Most surprisingly, is the demonstration of a complex coupling design of 'blazed' gratings, discovered by the EA with reduced restrictions on the device geometry. This approached coupled over 50% of the light at a normal incidence without use of a back reflecting layer. The unrestricted coupling gratings have a factor of 7 improvement over periodic gratings in their coupling efficiency.

The EA demonstrates that known solutions to a device design with periodicity can be consistently discovered with no preconditioning, or set periodicity. Even more impressive are the improvements in the device performance with small geometrical perturbation which break the periodicity, some not yet discovered in 'manual' optimizations in case of waveguide reflector Fig. 5.13.

Complex mathematical optimization schemes exist to attempt inverse electromagnetic problems. Their complexity and specialization require an in depth understanding by the user and potentially time consuming tuning for different design problems. The efficiency, robustness and minimal interference from a designer could potentially give an advantage to EA, when a wide variety of design parameters are to be explored.

CHAPTER 6

WAVEGUIDES AND CAVITIES: THEORY

6.1 Introduction

In order to design and study photonic cavities we must first begin with Maxwell's equations and briefly derive the basics of light confinement and propagation in waveguides and cavities. We will also discuss nonlinear aspects of light matter interaction and how that relates to experimental observations and cavity design.

All aspects of the electromagnetic wave propagation are completely described by generalized Maxwell's equations [34]:

$$\begin{aligned} \nabla \cdot B = 0 \qquad & \nabla \times E + \frac{\partial B}{\partial t} = 0 \\ \nabla \cdot D = \rho \qquad & \nabla \times H - \frac{\partial D}{\partial t} = J \end{aligned} \tag{6.1}$$

where,

$$D = \epsilon_0 \epsilon E + \chi^{(2)} E^2 + \chi^(3) E^3 + O(E^4) \qquad B = \mu H. \tag{6.2}$$

In the context of this thesis we assume the light is traveling in a mixed isotropic dielectric medium. In this material there is no free charge or current $\rho = 0, J = 0$, and the scalar relative permittivity $\epsilon(\mathbf{r})$ is a function of a cartesian position vector $\mathbf{r}$. Note, that the relative permittivity is just the square of the refractive index n. The scalar permeability μ is assumed to be constant and equal to the vacuum permeability $\mu_0 = 4\pi \times 10^{-7}$. Assuming that we are operating in a low power regime, we can neglect all of high order terms in the displacement

equation 6.2. We further simplify the equations by expressing displacement and magnetic induction fields in terms of the macroscopic electric and magnetic fields,

$$\begin{aligned} \nabla \cdot H(\mathbf{r},t) = 0 \qquad & \nabla \times E(\mathbf{r},t) = -\mu_0 \frac{\partial H(\mathbf{r},t)}{\partial t} \\ \nabla \cdot \epsilon(\mathbf{r}) E(\mathbf{r},t) = 0 \qquad & \nabla \times H(\mathbf{r},t) = \epsilon_0 \epsilon(\mathbf{r}) \frac{\partial E(\mathbf{r},t)}{\partial t} \end{aligned} \tag{6.3}$$

Since Maxwell's equations are linear we can split the temporal and spatial dependence by expanding the fields as a set of functions which vary sinusoidally in time. The general form of a field mode can now be written as function of space times a complex exponential. We can relate the complex field mode to a physical field by taking the real part of the $E(r,t)$ or $H(r,t)$.

$$E(\mathbf{r},t) = E(\mathbf{r}) e^{-\imath\omega t} \qquad H(\mathbf{r},t) = H(\mathbf{r}) e^{-\imath\omega t} \tag{6.4}$$

If we substitute these solutions into the divergence equations we get:

$$\nabla \cdot E(\mathbf{r}) = 0 \qquad \nabla \cdot H(\mathbf{r}) = 0. \tag{6.5}$$

The zero of divergence implies any field solutions must be made up from transverse plane waves. So for the electric field, $E(\mathbf{r}) = \mathbf{P} \cdot e^{\imath \mathbf{k}\cdot\mathbf{r}}$ implies $\mathbf{P}\cdot\mathbf{k} = 0$, where $\mathbf{k}$ is the wave vector, and $\mathbf{P}$ is the polarization vector. The curl equations 6.3 can also be separated by taking curl of both sides in one equation and substituting into the right hand side the curl of the other equation.

$$\nabla \times \nabla \times E(\mathbf{r},t) = -\mu\epsilon \frac{\partial^2}{\partial t^2} E(\mathbf{r},t) \tag{6.6}$$

The equation above can be transformed with vector identities to approximately equal,

$$-\nabla^2 E + \frac{1}{c^2}\frac{\partial^2}{\partial t^2} E = -\frac{4\pi}{c}\frac{\partial^2 P}{\partial t^2} E \tag{6.7}$$

in its final general form [34].

6.2 Waveguides

Now that we established the general form of solutions to Maxwell's equation in a dielectric medium, we can consider light confinement in a waveguide. A high index dielectric surrounded by a lower index one can confine light by total internal reflection. This hinges on the principle that light incident on an interface from the higher index side will be completely reflected if it strikes the surface above the critical angle. The critical angle is,

$$\theta_c = \sin^{-1}(\frac{n_h}{n_l}), \tag{6.8}$$

which is readily derived from Snell's law of refraction. One can readily imagine a ray of light being guided by bouncing inside of a large glass pipe. Once the pipe shrinks to the scale the light wavelength, we consider what happens due to the wave nature of light. In general we can think of the light pipe as a dielectric function of space with a continuous translational symmetry, $\epsilon(\mathbf{r}) = \epsilon(\mathbf{r} + m \cdot \mathbf{k})$. This implies light traveling in the pipe must also possess continuous translational symmetry. We can also argue from orthogonality of the solutions that for a given frequency of light there are is a discrete number of modes. We suppose the waveguide has a direction $\mathbf{k}$ and there is at least a single mode,

$$E(\mathbf{r}) = E_{\perp}(\mathbf{r}) \cdot E_{\parallel}(\mathbf{r}) \cdot e^{\imath\omega t} \tag{6.9}$$

, where we separate the spatial components of the mode into components parallel and perpendicular to the direction of the waveguide. If we apply the continuous translation symmetry condition to the solution, we find the parallel component can only have a phase variation along $\mathbf{k}$. If we look at a slightly different frequency $\omega + \delta\omega$, its reasonable to assume there is some perturbation to the field and there is a mode $E + \delta E$. The different modes must be orthogonal to

each other, which is not the case be cause $E \cdot (E + \delta E) = E \cdot E + E \cdot \delta E$. The first term in the product is unity and the second must be finite since the integration is over a localized region around the waveguide. A more detailed argument can be found in []. A series of modes for a waveguide are usually indexed with a decreasing wave vector (increasing eigenvalue). For a given frequency ω and a mode wave vector k, the phase velocity of a mode is $v_p = \omega/k$. The effective index of light propagating at phase velocity, v_p, is n_{eff}. The group velocity is similarly defined as $v_g = \frac{d\omega}{dk}$.

6.3 Traveling Wave Cavities

A waveguide bend into a ring with sufficiently large radius will have a resonant mode at a given frequency if an integral number, m, of wavelengths can fit along the circumference of the ring, L, $m \cdot \lambda = L \cdot n_{eff}$, where λ is the wavelength of light in vacuum. It can be shown that the spacing between resonant modes of the same order in a ring cavity is $\delta\lambda = \lambda^2/n_g L$. This spacing is commonly called the free spectra range (FSR). A resonant mode in a cavity decays with a life-time of τ and resonance frequency ω. We define the quality factor of a resonator as the ratio of energy stored in the cavity divided by power dissipated in one round trip in the cavity. Q can be written as, $Q = \omega\tau/2$, and in frequency domain $Q\omega/\delta\omega$, where $\delta\omega$, is the spectral width at half maximum. The later expression of Q is especially useful, since the resonance frequency and full width at half transmission intensity is readily measured from the optical transmission spectrum of a coupled cavity. We can view a ring cavity coupled to a waveguide simply as a four port system, Fig. 6.1. The incoming field amplitude A_0 is partially transmitted $A_1 = t \cdot A_0$, and partially coupled to the waveguide ring $B_1 = \imath r \cdot A_0$. The

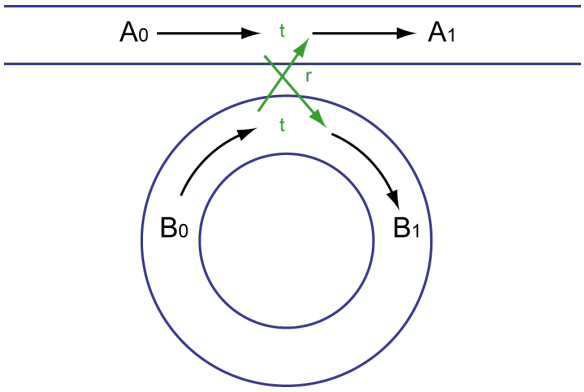

Figure 6.1: Waveguide coupled to a ring.

light in the ring undergoes a phase shift and some attenuating during a single trip around the length, L, of the cavity, $B_0 = B_1 \cdot e^{\imath kL} = B_1 \cdot e^{\imath k_r L} \cdot e^{-k_i L}$. We can write equations for all the amplitudes involved in matrix form as an eigenvalue problem.

$$\begin{pmatrix} 1 & 0 & 0 & 0 \\ 0 & 0 & e^{ikL} & 0 \\ ir & t & 0 & 0 \\ t & ir & 0 & 0 \end{pmatrix} \cdot \begin{pmatrix} A_0 \\ B_0 \\ B_1 \\ A_1 \end{pmatrix} = \lambda \begin{pmatrix} A_0 \\ B_0 \\ B_1 \\ A_1 \end{pmatrix} \tag{6.10}$$

This system is readily solved and yields the transmitted amplitude, and the amplitude inside the cavity both normalized to the amplitude coupled into the system, A_0.

$$A_1 = \frac{e^{ikL} r^2 + e^{ikL} t^2 - t}{e^{ikL} t - 1} \tag{6.11}$$

$$B_1 = \frac{ir}{1 - e^{ikL} t} \tag{6.12}$$

We observe that inside the cavity, on resonance, the field power is $\frac{r^2}{(1-e^{-Lk_i}t)^2}$. The e^{-Lk_i}, is the amplitude after one roundtrip in the cavity. If we assume coupling coefficient t is equal to the amplitude transmission after one roundtrip (critically coupled), and that coupling magnitudes add up to unity, $t^2 + r^2 = 1$, the power on resonance inside of the cavity is $1/(1 - t^2)$. With above conditions, the power

transmitted on resonances is equal to zero. We refer to power enhancement inside the cavity as Finesse, which under critical coupling conditions is,

$$F = \frac{FSR}{\delta\lambda}. \tag{6.13}$$

6.4 Dispersion

Dispersion is the spread of pulse in time as it propagates. A pulse has a finite spectral range, and unless it is moving through vacuum, different frequencies in the pulse see a different material refractive index. After propagating some distance and reaching a detector, the spread in pulse width is called the group velocity dispersion. Most dielectrics in the visible and telecommunication range have normal dispersion, meaning refractive index decreases with longer wavelengths. The opposite of normal is anomalous dispersion, and the wavelength where dispersion changes from normal to anomalous is called the zero group velocity dispersion point. If we assume propagation through a wavelength scale waveguide, which supports only a single propagation mode, the effective index of the traveling mode can strongly depend on the exact waveguide dimensions if the difference between the refractive index of the waveguide and the surrounding material is high ($\triangle\lambda > .1$). The dispersion seen by a single waveguide mode is called waveguide dispersion. It has been already shown for very high index contrast waveguides like silicon in silicon oxide, that anomalous dispersion crated by the waveguide can counter the material dispersion of silicon yielding a spectral range with close to zero dispersion, and even a zero dispersion point. A waveguide bent into a ring will have a different dispersion than a straight waveguide with the same cross section, since guided mode in

the ring is shifted slightly to the outside of the ring. Hence it is possible to tailor dispersion in a ring cavity by changing the cross section shape as well as the radius of the ring.

6.5 Nonlinearities

We return to the initially truncated terms in Eq. 6.2. The terms, $\chi^{(2)}$ and $\chi^{(3)}$ are called second and third order optical nonlinear susceptibilities. The third order nonlinear polarization corresponding to $\chi^{(3)}$ is dependant on the cubed amplitude of the field. Most generally the term is a tensor describing interaction of four wavelengths. In the case of centro-symmetric materials, the tensor only has significant non zero values for fields polarized in the same direction. The second order nonlinear nonlinear polarization is $\chi^{(2)}$, and is only present in non centro-symmetric materials.

In the presence of two polarizations and $\chi^{(2)}$, wave mixing process can occur such that the two photons with frequencies ω_1, ω_2 are converted into a single photons of with frequency ω_3. Energy conservation implies $\omega_1 + \omega_2 = \omega_3$. The process has vast application, since it implies that a single laser frequency can be converted to an arbitrary pair of frequencies as long as energy is conserved. We can combine Eq. 6.7 for light traveling in the z direction, and the nonlinear displacement Eq. 6.2 to arrive at,

$$\left(\frac{d^2A_3}{dz^2} + 2ik_3\frac{dA_3}{dz} - k_3^2A_3 + \frac{\epsilon\omega_3^2A_3}{c^2}\right)e^{i(k_3z-wt)} + c.c. = \frac{-16\pi d_{eff}\omega_3^2}{c^2}A_1A_2e^{i(k_1+k_2)z-\omega_3t} + c.c. \tag{6.14}$$

The A_ns and k_ns, are the amplitudes and wave vectors of ω_ns polarizations. The d_{eff} term is just $\chi^{(2)}/2$. We typically assume the second derivative term is small

and can be neglected, and $k_3^2 = \frac{\epsilon\omega_3^2}{c^2}$, yielding,

$$\frac{dA_3}{dz} = \frac{-8i\pi d_{eff}\omega_3^2}{c^2 k_3} A_1 A_2 e^{i\Delta kz} \tag{6.15}$$

We define $\Delta k = k_1 + k_2 - k_3$, which is called the wave vector mismatch. We see that with zero mismatch the sum frequency amplitude, A_3, will experience continuous growth until the A_1, A_2 fields become depleted. In the presence of finite mismatch, the A_3 term will cycle sinusoidally through growth and depletion and never experience overall growth.

Third order nonlinearity gives rises to nonlinear interaction of four polarizations. In the case of two polarizations being identical, the energy conservation yields $\omega_1 + \omega_1 = \omega_2 + \omega_3$. Where, the first frequency is the pump frequency and the two other frequencies are generated. Similarly to the $\chi^{(2)}$ process, a wave vector, or a phase mismatch is defined as $\Delta k = 2k_1 - k_2 - k_3$. This phenomena is called optical parametric conversion. Usually the goal is to convert a pump frequency to two new nearly spaced frequencies .

Since the generation efficiency depends on the square of the power, high finesse cavities are an ideal environment for high efficiency parametric conversion. In a ring cavity excited in mode m, modes spaced same number of increments of m above and below are innately phase matched since,

$$L = m\lambda_m/n_{eff,m} = (m + x)\lambda_m/n_{eff,m+x} = (m - x)\lambda_m/n_{eff,m-x}, \tag{6.16}$$

and it follows,

$$n_{eff,m+x}/\lambda_{m+x} = L(m + x), n_{eff,m-x}/\lambda_{m+x} = L(m - x), \tag{6.17}$$

hence the sum of those terms is,

$$n_{eff,m+x}/\lambda_{m+x} + n_{eff,m-x}/\lambda_{m+x} = L(m + x) + L(m - x) = 2Lm = 2n_{eff,m}/\lambda_m, \tag{6.18}$$

and phase matching is satisfied. Unfortunately, unless the resonances are spaced evenly in frequency, energy is not necessarily conserved. However, if the pump resonances is in a zero group velocity dispersion point in the spectrum, the resonant modes immediately above and below it are spaced equally in frequency. For this condition to be satisfied the cavity must be carefully designed to cancel material dispersion with waveguide dispersion in the ring [28, 1, 16, 38, 60].

We consider the sum frequency Eq. 6.15 again for light propagating through a waveguide with width changing as a function of position. The intensity of light in the waveguide will slightly change with different widths, and we assume the change on effective index is negligible. We also consider the case where $A_1 = A_2$, or the case of second harmonic generation. For a sinusoidal variation in width with period Λ we assume a sinusoidal variation in intensity, yielding,

$$\frac{dA_3}{dz} = \frac{-8i\pi d_{eff}\omega_3^2}{c^2 k_3} A_1 A_1 (1 + A_m Cos(2\pi z/\Lambda)) e^{i\Delta k z}. \tag{6.19}$$

The amplitude of intensity modulation is small $A_m \ll 1$, and oscillatory part of the equation can be rewritten as a set of exponentials,

$$\frac{dA_3}{dz} = \frac{-8i\pi d_{eff}\omega_3^2}{c^2 k_3} A_1 A_1 (e^{-i\Delta k z} + \frac{1}{2} A_m e^{-i(\Delta k + \frac{2\pi}{\Lambda})z} + \frac{1}{2} A_m e^{-i(\Delta k - \frac{2\pi}{\Lambda})z}). \tag{6.20}$$

In the last exponential we consider the case when, $\Delta k - \frac{2\pi}{\Lambda} = 0$, the zero in the exponential simplifies the final equation to,

$$\frac{dA_3}{dz} = \frac{-8i\pi d_{eff}\omega_3^2}{c^2 k_3} A_1 A_1 (e^{-i\Delta k z} + \frac{1}{2} A_m e^{-i(\Delta k + \frac{2\pi}{\Lambda})z} + \frac{1}{2} A_m). \tag{6.21}$$

Now the rate of growth of the generated second harmonic is a sum of oscillating terms and a constant. This means there is an overall growth in the generated light, as the pump frequency propagates through the waveguide. Hence, we no

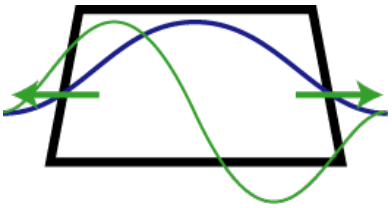

Figure 6.2: Cross section of a waveguide. The blue curve is transverse mode profile of fundamental TE mode of wavelength λ. The green arrows are polarizations induced by the field in the primary mode at the walls, the induced polarization is twice the frequency of the main field. The green curve is the transverse mode profile of second order mode of the second harmonic, $\lambda/2$.

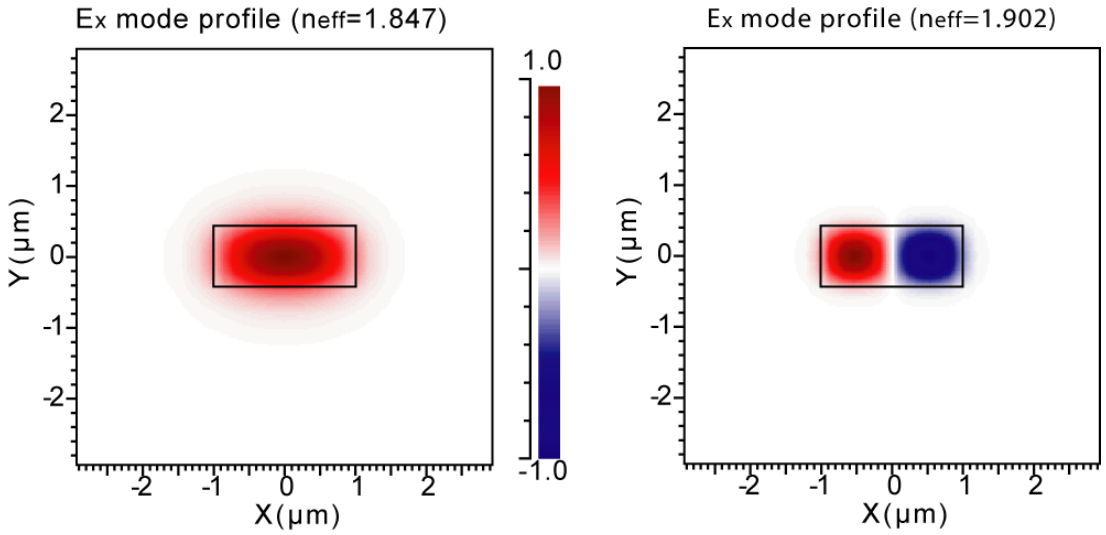

Figure 6.3: Waveguide modes for 2.0x0.74 micron waveguide, stoichiometric silicon nitride core, silicon oxide cladding. (a) 1550 nm wavelength fundumental TE mode, (b) 775 nm second order TE mode, $\lambda/2$.

longer need to satisfy the phase matching condition $\Delta k = 0$, to have net gain in the second harmonic as long as the quasi phase-matching period Λ,

$$\Lambda = \frac{2\pi}{\Delta k} = \frac{2\pi}{4\pi n_{eff,\lambda}/\lambda - 2\pi n_{eff,\lambda/2}/\lambda}, \tag{6.22}$$

is satisfied. A more detailed discussion and derivation can be found in [10].

We consider a specific case where a $\chi^{(2)}$ effect could be observed. Consider the fundamental mode of TE polarized light in a waveguide. The confined mode has strong overlap with the waveguide walls. The field normal to the waveguide walls sees a non centro-symmetric medium at the wall interface. This type of medium has an innate $\chi^{(2)}$. Hence, a symmetric mode (blue curve in Fig. 6.2) propagating in the ring waveguide cross section (black trapezoid Fig. 6.2) can produce a polarization vector across the interface at twice the pump frequency, green arrows in Fig. 6.2. The generated light must have an anti-symmetric mode profile be cause polarizations on the opposite walls will have opposite phase, green curve Fig. 6.2. Using a mode solver we calculate an effective index of a 1550 nm fundamental mode, Fig. 6.3(a) and the anti symmetric TE mode of the second harmonic 775 nm, Fig. 6.3(b). From those values and we find $\Lambda = \lambda/(2 * 1.902 - 2 * 1.847) \sim 14$ microns.

CHAPTER 7

WAVEGUIDES AND CAVITIES: DESIGN AND FABRICATION

7.1 Introduction

Integrated photonic devices are fabricated on small dies (~5x20 mm) and are tested by coupling light in through a tapered fiber and collecting the output with another fiber or a microscope objective on the opposite side of the die, Fig. 8.1. The light is coupled in and out of the waveguide by adiabatically tapering down the width of the waveguide before it terminates at the edge of a die. This device measurement scheme allows for many waveguides to be on a single die arranged in parallel to each other.

Typically several aspects of the device geometry are varied to measure their effect on optical performance of the device and to accommodate for fabrication variations. Usually we vary cavity radius, waveguide widths and gap between a coupling waveguide and a cavity. For generation of layouts of microelectronics devices a number of mature software tools exist to automate the process. For photonic devices however, there is a lack of software tools to accommodate the unique needs like curved waveguides. We developed a general function library to simplify and automate layout generation for photonic devices. A detailed description of its capabilities can be found in Appendix A.

7.2 Design

We design ring cavities with radii of ~20 um, height of 300 nm to over 700 nm, and width of 700-1600 nm coupled to a bus waveguide of the same dimensions. The devices are clad on top and bottom with 3-5 microns of silicon dioxide. The difference between TE and TM effective indices was ~0.03 and higher for above dimensions and minor field component in both polarizations was <10% of the orthogonal major field components. The rectangular cross section was chosen to minimize coupling between the polarizations. The measurement of transmission spectrum of the waveguide coupled rings showed distinct TE and TM resonances with high (>20 dB) extinction for both resonances, ensuring polarization stability.

We also fabricated a set of modulated rings and waveguides in order to observe the effects of $\chi^{(2)}$. The width of the waveguide was sinusoidally changed modulated with period Λ. The modulated waveguide had a length of 1 cm. The radius of modulated rings was 20 microns, Fig. 7.1.

7.3 Fabrication

We fabricate our devices on 4" silicon wafers with 3-5 microns of thermally grown SiO_2. Stoichiometric silicon nitride is deposited in a low pressure chemical vapor deposition (LPCVD) oven. The designs of photonic structures are patterned using electron beam lithography (EBL). An inductively coupled plasma reactive ion etcher (ICP RIE) is used to etch the devices into silicon nitride with EBL resist as a mask. Devices are annealed after patterning in a high temper-

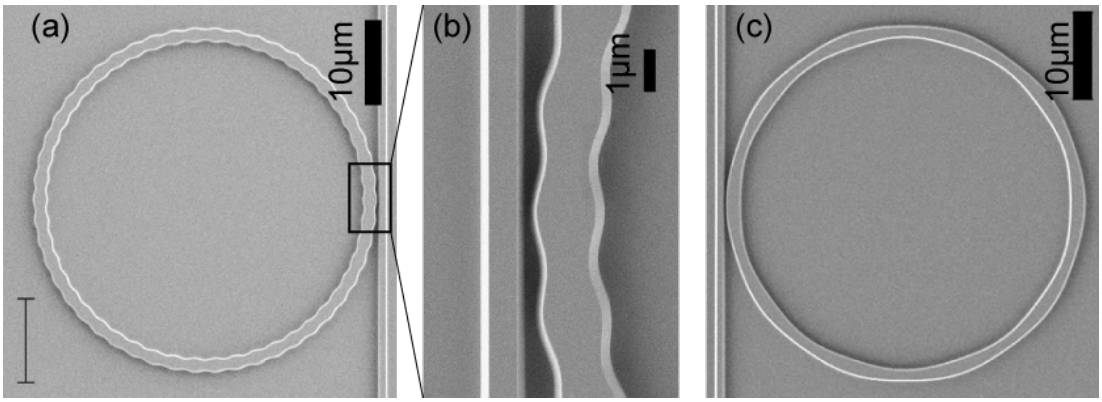

Figure 7.1: Micrographs of width modulated rings: (a) 3 micron period, (b) magnified coupling region of 3 micron period ring, (c) 14 micron period for quasi phase matching. The waveguide height is 740 nm. The rings are etched from stoichiometric silicon nitride. The micrograph is taken before cladding with SiO_2.

ature over (1200C). The annealed devices are covered with SiO_2 using a high temperature oxide (HTO) oven, and plasma enhanced chemical vapor deposition (PECVD) tool.

7.3.1 Materials

A wide variety of materials are readily available for integrated photonics. Crystalline silicon, silicon oxide, silicon nitride and silicon oxynitride are commonly used in CMOS fabrication of electronics. Silicon and silicon oxide are the most common materials in sub micron photonics but are limited to the infrared spectrum due to the bandgap of silicon. High tensile stress and lack of electrical conductivity in silicon nitride has kept it from being widely studied for photonic applications with some exceptions. We concentrated on nitride as our material of choice be cause of its versatility and low linear and nonlinear absorption.

Silicon Dioxide

Silicon dioxide (oxide) is a versatile low index dielectric for photonic devices due to its transparency in the visible and infrared wavelengths. Low nonlinearity and ease of deposition, make for a widespread use in microfabrication. Oxide can be deposited via LPCVD, PECVD or it can be grown on silicon via thermal oxidation.

Growth by thermal oxidation of crystalline silicon produces the highest quality, dense oxide without adding impurities. The process requires high temperature, 900-1200° C. The grown film is conformal and stable when annealed at hight temperatures. Lack of voids and impurities makes thermal oxide ideal for low loss photonic applications. PECVD deposition is most commonly used to create thick oxides at relatively low temperatures, 200-400° C. The deposited film is formed by ionization of SiH_4 and N_2O. The formed filmed contains hydrogen impurities from the silane precursor. The film is not conformal and contains voids. With high temperature annealing the hydrogen is outgassed and the film densifies.

High temperature chemical vapor deposition is an LPCVD process which takes place at 800-900° C with N_2O and $SiCl_2H_2$ precursor gasses. The film is conformal and contains chlorine impurities. With high temperature annealing the impurities are outgassed. The deposition is conformal and produces higher quality films in comparison to the PECVD process.

Stoichiometric Silicon Nitride

Silicon nitride (Si_3N_4) is a versatile high index dielectric for photonic devices due to its low nonlinearity [32] and its transparency in both the visible and infrared spectrum [51, 21, 62]. To date silicon nitride waveguides have not been widely employed for propagation in the infrared. The main barrier is the high tensile stress, which limits the thickness of low pressure chemical vapor deposited (LPCVD) Si_3N_4 films to ~250 nm [15, 7, 20, 74]. The thin film limits the lowest loss modes to quasi-TE (electric field polarized in the substrate plane) which are poorly confined in the nitride and have a very small effective mode index (neff) ¡ 1.6, and a large, ~5 micron MFD. Highly delocalized waveguides in the C-band have been demonstrated with losses as low as 0.1 dB/cm [63] and rings, with diameters as large as several millimeters, have been shown with quality factors as high as $2.4*10^5$ [29]. In the visible spectrum, Adibi et al. demonstrated structures with Q's over $4*10^6$ at wavelength of 655 nm [31]. Plasma enhanced chemical vapor deposition (PECVD) has been recently optimized to deposit Si_xN_y nitride films at low temperature (400C) with losses below 1 dB/cm at wavelength of 532nm [26]. The film also contains hydrogen impurities which have detrimental effects on absorption in the near infrared. High temperature anneal of the nitride film at 1200° C removes some of the stress and outgasses trapped gasses. By cycling depositions of 300 nm nitride films at 800° C and 1200° C annealing cycles, films over 700 nm were successfully deposited. Caution must be taken when etching high stress film from one side of the wafer. The stress from the unetched side of the wafer is left unbalanced and can lead to film cracking and wafer breaking. To avoid this problem we etched features halfway through on the patterned side. Before finishing the primary pattern etch on the front of the wafer, we etched all of the nitride from the back

of the wafer. This prevents excessive bending of the wafer during fabrication and reduces surface cracking. PECVD deposition of nitride is used if low operating temperature is required. The deposited film tends to be of a lower optical quality, but recently a significant progress has been done in optimizing PECVD systems for nitride as mentioned in first paragraph of this section.

7.3.2 Electron Beam Lithography

Electron beam lithography (EBL) utilizes a high voltage (100 kV) electron beam to expose a thin film of E-beam resist. The resist is chemically developed and used as a fabrication mask in further steps. The electron beam can be focused to 1 nm diameter, allowing for high resolution patterning. The beam is deflected across the sample by a set of electrical coils in discrete steps (2-10 nm) to define a pattern. To pattern the resist, it must be exposed at a certain charge density (dose) via the electron beam, hence write time is inversely proportional to the beam current. We utilize JEOL 9300, and Leica VB6 E-beams for the pattern writing. Both tools typically usually operate in the 1-2 nA beam current range. We increasing the current to 10-25 nA to reduce write time on the tool. Conveniently, at high currents the spot size of the beam increases. The large diameter of a high current electron beam blurs the pixelation of the curved features in the rings and waveguide bends.

Positive and negative resists can be used in EBL. In positive resists, the unexposed regions remain, and in the negative resists the exposed regions are preserved. Since waveguides and cavities take up a very small fraction of wafer area, a negative resist is desirable to decrease EBL writing time. We found MaN

negative resist to be most versatile for fabrication of waveguides and cavities. It can be readily used to pattern features 25 nm and smaller in size, and has relatively low feature size dose dependency. *Surpass 3000*© is used as an adhesion promoter on nitride and oxide before MaN can be properly deposited. Surpass is applied with spin deposition by first flowing deionized water on a wafer spinning at 250 RPM. While wafer is spinning and still wet the surpass is flowed for 20 seconds out of a 60cc syringe without a plunger. Deionized water is flowed again over the spinning wafer for 30 seconds, and wafer is dried by spinning up to 2000 RPM.

The E-beam resist is spun on the Surpass treated wafer at 1500 RPM for 30 seconds. For consistency we filtered the resist through 0.2 micron syringe filters onto the wafer before spinning. The resist is baked at 90-110° C for 1 minute. The wafer is spun with E-spacer for 1 minute at 1500 RPM. E-spacer prevents charge buildup in the dielectric during EBL. Pattern is written with EBL using a $700mC/cm^2$ dose. Dose can be increased up to $1200mC/cm^2$ if the feature size is 100 nm or smaller. After exposure wafers are developed in a Hamatech developer tool in MIF300 developer for 90 seconds. After development, residual traces of resist are left behind in unexposed regions and must be removed with a light oxygen plasma. Patterned resist will exhibit roughness which will increase scattering in patterned photonic devices. Placing wafer on hotplate at 145° C for 5 minutes will cause densification of the resist, and reflow of the resist surface, significantly decreasing roughness. The wall shape and angle can be deformed by the reflow process depending on the width of the feature, Fig. 7.2. Densification of the resist also decreases its etch rate, a helpful side effect when etching thick oxide or nitride films over 300 nm thick. In the Oxford 100 etch tool 3.3:1 etch ratio between nitride and resist is typically achieved with a CHF_3O_2 and

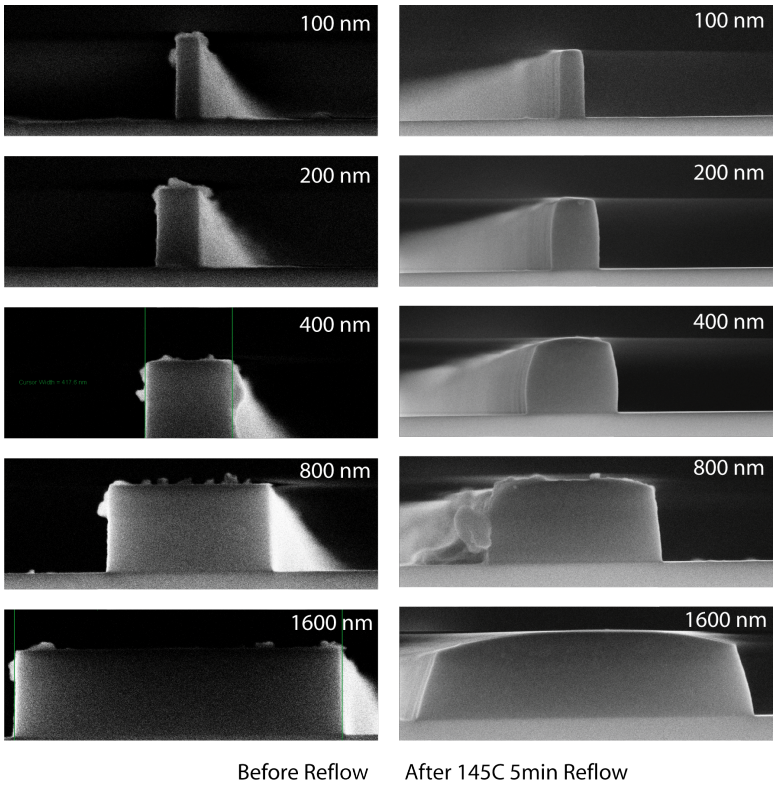

Figure 7.2: Micrograph of resist cross sections before and after reflow. Resist reflow smooths the sidewalls and shrinks the resist, forming sloped or bubbled sidewalls depending on the width of the features. The resist underwent a pre exposure bake at 110° C to minimize shrinking effect of the reflow.

O_2 etch chemistry.

7.3.3 Etching

Etching of silicon dioxide and silicon nitride films can be done by reactive ion etching (RIE), or inductively coupled plasma reactive ion etching (ICP RIE). The usual precursor gasses are SF_6, CHF_3O_2, CF_4 and O_2. Argon, helium and and nitride dilution gasses are sometimes added to slow down the etch rate. In RIE etching occurs in several step. First, CHF_3O_2 or CF_4 are dissociated by impact

with energized plasma electrons and other particles. The breakup produces reactive species including CF_3^+, F and others. The reactive species diffuse into the solid where they are adsorbed into the surface, breakup bonds with silicon, form SiF_4 and finally leave the surface. If oxygen is present in the plasma, it speeds up the etch by oxidizing the silicon on the sample surface. Silicon oxide more readily adsorbs fluorine ions and etches almost twice as fast as nitride. An inductively coupled power source generates plasma in an ICP etcher. The source creates high density, low pressure, low energy plasmas by coupling electrons into the magnetic field produced by the RF voltage. The higher electron density allows for faster etching with a low sidewall angle. Generally higher RF power in an etcher decreases side wall angle and increases roughness and etch rate. In etch chemistry where polymerization can occur (like CHF_3O_2 and O_2), increasing percentage of oxygen will decrease polymerization. The higher oxygen content consumes the formed polymer and expedites removal of resist and hence decreases selectivity. The ICP and RIE powers, as well as gas pressure and chemistry are optimized to balance etch roughness, sidewall angle, etch selectivity to masking material and etch speed.

7.3.4 Annealing

High temperature annealing decreases absorption and scattering losses in thin films. Deposited materials hold elements of their precursor gasses which failed to escape during material deposition. Impurities like hydrogen and oxygen form bonds with silicon and nitride atoms. Those bonds absorb in the infrared bands and introduce significant losses to the propagating light. Annealing etched devices at sufficiently high temperatures forces the trapped gasses

to escape out of the material. During high temperatures reflow and densification of thin films also occurs. Denser films have fewer voids and are more homogenous, and consequently have less scattering sites. We anneal etched silicon nitride devices in a high temperature oven in a nitrogen atmosphere for 3 hours at 1200° C.

7.3.5 Miscellaneous Processing

Resist densified by reflow and etched in and RIE or ICP etcher can be stubborn to typical acetone and isopropyl alcohol removal attempts. Complete removal of leftover resist is achieved by placing the sample in a oxygen plasma tool. Caution must be taken if an etcher is used for the process, if the wafer chamber is not thoroughly cleaned by an aggressive oxygen plasma process, reactive gasses deposited on chamber walls may continue to etch the sample. The substrate temperature in the plasma chamber must be raised to 150° C or higher temperature to insure complete removal of the resist. Dies with fabricated devices have to be cut from the finished wafers in order to be tested. Since light is coupled in and out of the edges of the dies, the final dicing step is critical to the insertion losses of the devices. We used a dicing saw with a spinning circular blade to cut apart out wafer. We found that by using a sufficiently thin diamond coated blade the residual roughness was on the order of 2 microns RMS. The edges of the die could be further polished with a lubricant slurry using a 1 micron and 0.5 micron rough polishing pads to decrease insertion loss by 1 dB/facet. Depending on the geometry of the taper a final polish increased back reflection of light exiting the waveguide.

CHAPTER 8

WAVEGUIDES AND CAVITIES: EXPERIMENTAL RESULTS

8.1 Experimental Setup

Integrated devices were tested by coupling light in one facet of a chip through a tapered fiber with a 5 micron spot focus diameter, and collecting light from the output waveguide on the opposite side of a chip with a microscope objective. The general outline of the testing setup is in Fig. 8.1. The output of a microscope objective was either focused on a NewPort 818-IR detector or collimated into a fiber with a collimator attachment. The fiber was connected to an optical spectrum analyzer. The coupling fiber holder was mounted on a 3 axis piezo stage, which was mounted on a 3 axis translation stage with differential micrometers. The device die under test was placed on an aluminum block mounted on a 2 axis tilt stage. The tilt stage was on top of a rotation stage. The rotation stage was on a single axis translation stage, the translation axis had a 5 cm range and was perpendicular to the coupling fiber. The microscope objective was mounted on a 3 axis translation stage. The piezo was computer control for fine alignment. A feedback loop measured transmitted power from the NewPort detector and moved the piezo to maximize transmission. A long working distance (2.5 cm), 10x microscope objective with an Olympus microscope column was placed to look straight down onto the chip. The column had a built in prism cube to couple a goose neck illuminaton fiber. On top of the microscope a Merlin InGaAs high sensitivity IR camera was placed to aid in coupling and observe scattering from waveguides and cavities.

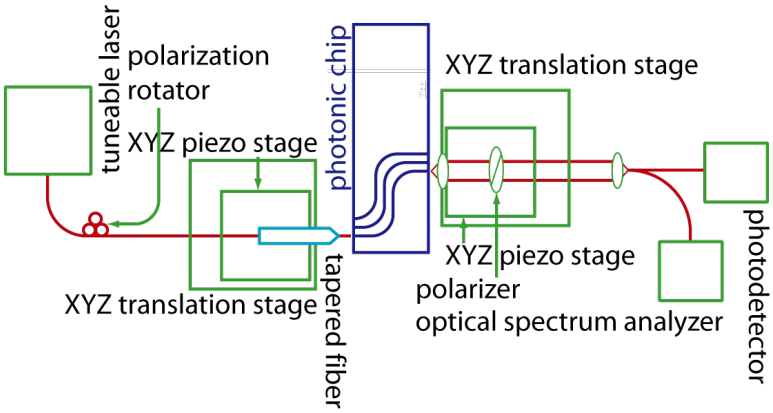

Figure 8.1: Configuration of testing setup as viewed from the top.

8.2 Results

8.2.1 Propagation Losses

In order to accurately distinguish between scattering and absorption losses, we introduce carefully engineered defects in the cavities and use Borselli's method [14] to extract linear absorption and scattering coefficients from the optical cavity spectrum. The method consists of measuring the shift of the cavity resonance as a function of the input power coupled into the ring, Fig. 3. The red shift is caused by the temperature increase in the cavity. The temperature change is only dependent on the absorption coefficient (and not on the scattering). The resonance shift as a function of the input power is measured for several rings with different intrinsic quality factors to accurately calculate contributions from different loss mechanisms. The quality factor determines the degree of the built up energy in the ring, and therefore the dependence of the resonance shift with the input power. We measure the Qs of rings with different number of artificial defects and from the difference between Q's find that each scatterer contributes

0.150.05dB/cm of attenuation in the ring. Figure 3 shows the red shift of the resonances for one of the rings without defects. The slight asymmetry of the resonance at high input power is due to the bistability, typical of high Q rings. Figure 4 shows the extracted resonance shift from plots such as Fig. 3 for rings with different number of defects. The resonance shift shows strong linear dependence on the coupled power indicating low nonlinearities (Figure 4). Quadratic fit of resonance shift to power dropped indicates nonlinear losses were 2% of total losses in the cavity. We measure coupled Q for a ring without scatterers to be 244,000 with 70% transmission on resonance corresponding to intrinsic Q of 3,000,000 and an intrinsic attenuation coefficient of 0.12dB/cm. We estimate the scattering and absorption losses to be below .065dB/cm and .055dB/cm, respectively. These losses are extracted from the resonance shift dependence on the power dropped by the ring, P_d, given by $\delta\lambda(P_d) = C(\gamma_a/\gamma_t)P_d$, where C is the thermal coefficient of the effective index of the waveguide, $(\gamma_a/\gamma_t)P_d$ is the fraction of dropped power absorbed by the material in the cavity, is the absorption loss coefficient, and γ_t is the total loss coefficient in the cavity. The total loss coefficient is the sum of all losses $\gamma_t = \gamma_s + \gamma_e + \gamma_a$, where γ_s, is the loss due to scattering and γ_e is the unloading loss from the ring to the bus waveguide calculated from the measured low power transmission lorentzian line shape [14,15]. The shift over power ratio $\delta\lambda(P_d)/P_d = C(\gamma_a/\gamma_t) = S$ is extracted from Fig. 4 for the different rings. The thermal coefficient $C = 0.01$ pm/W is extracted from resonance shifts nonlinear dependence on dropped power by fitting a quadratic dependence of resonance shift on Pd. The absorption loss coefficient, P_d , is then found by extracting γ_a for each ring.

8.2.2 Optical Parametric Oscillations

We measured transmission through waveguides coupled to cavities designed to exhibit optical parametric oscillations. For a 58 micron radius cavity with a 711 nm waveguide height, a base width of 1700 nm and 20 degree sidewall angle. We tested the device using setup in Fig. 8.2. The measured Q was 500,000 and the spacing of first order TE modes was 3.2 nm. We 'thermally locked' the laser to a resonance at 1544.9 nm. To perform the lock we set the laser to a shorter wavelength and slowly increased the wavelength until transmission was close to a minimum. As the laser was coming into a resonance, the absorbed power in the cavity caused a temperature increase and a red shift in the cavity resonance. By tuning the laser slowly, we could achieve close to minimum transmission. In thermal equilibrium the heat dissipated by the die and the die mount is equal to heat created from absorption of laser radiation inside of the cavity. The cavity in this state is said to be locked, since heating of the cavity causes a resonance red shift, and hence a decrease in coupled power. With less coupled power, less energy is dissipated in the cavity causing it to cool back to original position. Similarly, if cavity resonance cools and shifts towards the laser wavelength, increased coupled power drives cavity back to original position. The output light from the thermally locked cavity was coupled into an optical fiber and measured with an optical spectrum analyzer, Fig. 8.2. We observed 61 new frequencies between 1450 nm and 1750 nm in Fig. 8.2a. Coincidentally this covers the S, C and L telecommunication bands. We repeated the same set of measurements for a smaller ring with a 20 micron radius, and a Q of 100,000 at a resonance of 1561 nm, Fig. 8.2b. We were able to observe 20 generated wavelengths. We measured the threshold of oscillations for a 40 micron radius ring with a Q of 200,000. We varied coupling power to the ring and measured output power

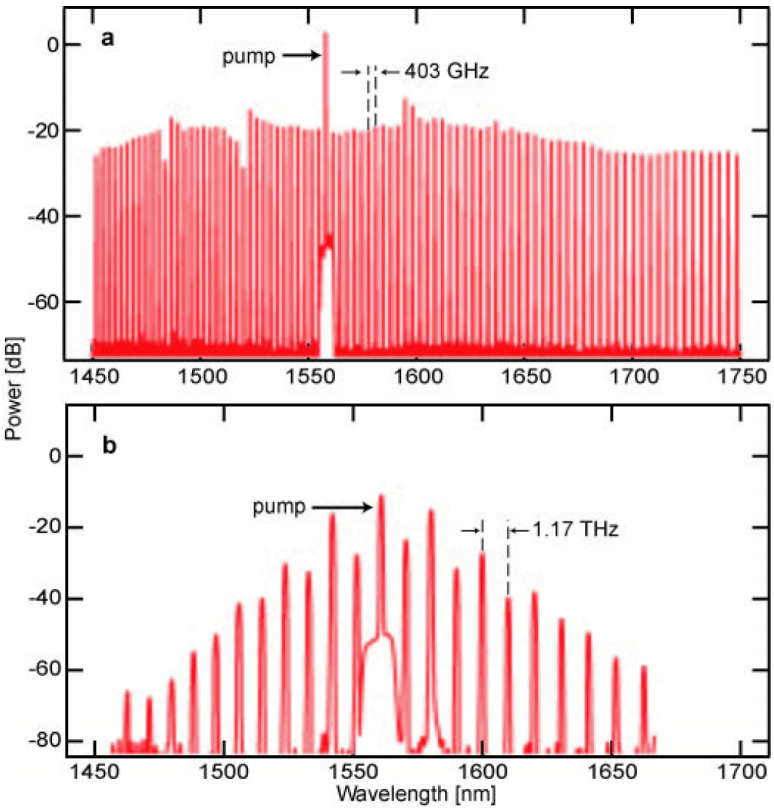

Figure 8.2: Spectrum of light generated by silicon nitride microring cavity coupled to a waveguide; (a) light generated by a 57 micron radius ring, (b) light generated ring with 20 micron radius.

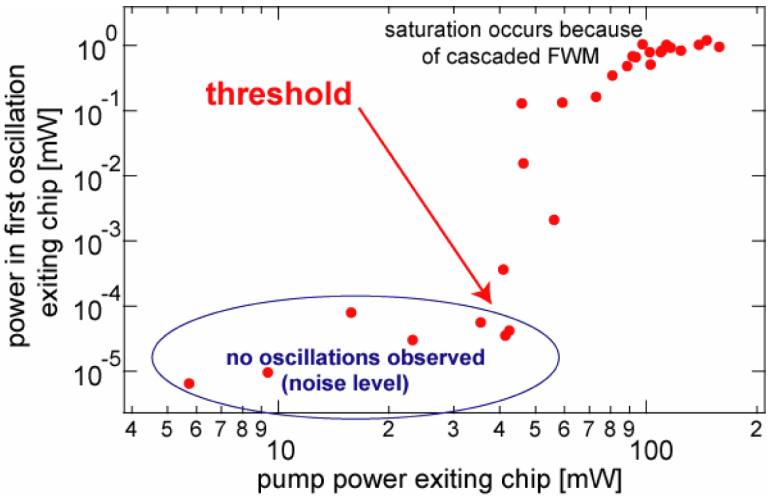

Figure 8.3: Measured output power from the strongest generated harmonic of the optical parametric oscillator.

in the strongest generated mode. The threshold of oscillation was 50 mW and above 100 mW the power generated in the strongest mode saturated, Fig. 8.3.

8.2.3 Harmonic Generation

We measured emission of second and third harmonic in our resonant cavities. The transmission for multiple rings is plotted in Fig. 8.4(a), where the vertical axis is the width modulation period of the ring. The third harmonic has been reported previously in micro cavities and is a result of the $\chi^{(3)}$ nonlinearity present in all centro-symmetric materials [11]. The emission of second harmonic is a result of $\chi^{(2)}$, and has not been previously shown in literature for integrated centro-symmetric based cavities. We suspect the break in translational symmetry occurs at the interface between the high and the low index dielectrics at the walls of the waveguide. We plot the measurements of light scattered from the top of a cavity in Fig. 8.4(b). For the collection of light we placed a detector and a microscope objective over the cavity. This method of measurement only collects a fraction of emitted radiation, and is not sufficiently accurate to find absolute generation efficiency. However, from the preliminary data we found that second harmonic power was three orders of magnitude higher compared to third harmonic, implying a significant effective $\chi^{(2)}$.

The ring cavities which exhibited quasi phase-matching modulation length as calculated in the previous chapter were the only ones emitting the second harmonic, which strengthens our belief that the nonlinearity is caused by the waveguide wall interface. To collect the second and third harmonics we used a silicon detector, which has a cut off at the silicon bandgap and hence does not

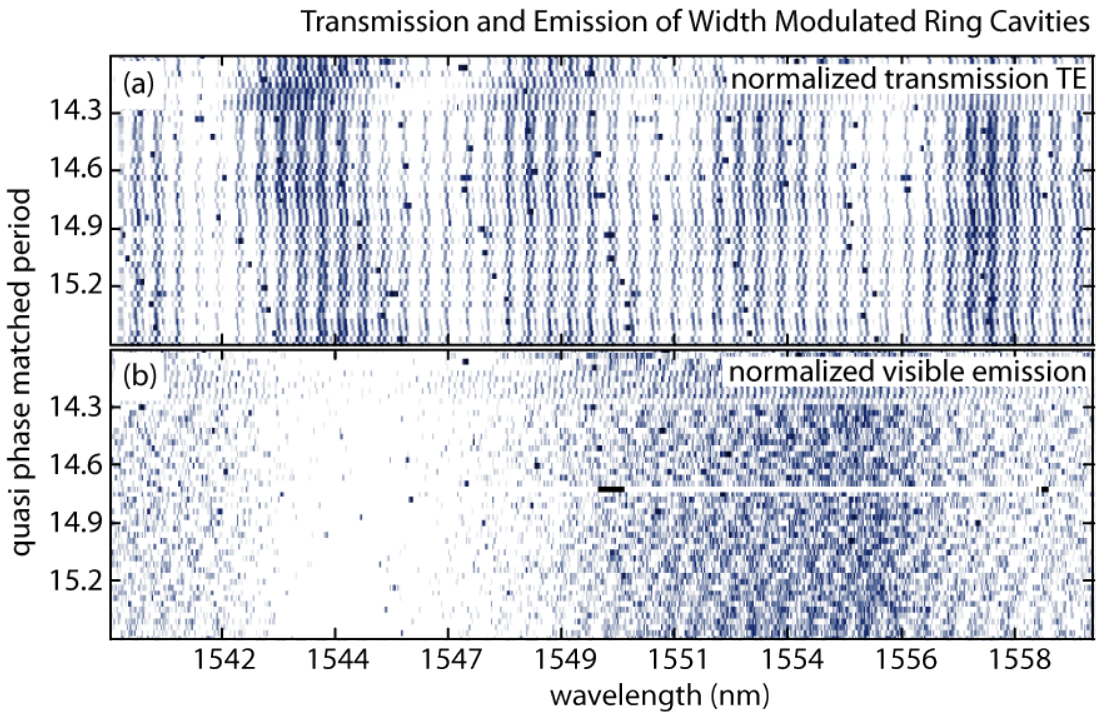

Figure 8.4: (a) Normalized transmission, (b) normalized visible emission of modulated ring cavities. The y axis in (a) and (b) is the quasi phase matching length, Λ, in the ring. The x axis in (a) and (b) is the wavelength of the laser. The power in waveguide is estimated to be 0.19 W. The emission in cavity $\Lambda = 14.72$ is a red (second harmonic), all other cavities emit green light (third harmonic).

pick up any of the pump light (1550 nm) scattered from the cavity.

8.3 Summary

The demonstrated silicon nitride devices in this work have the lowest loss and highest confinement to our knowledge in the near infrared spectrum. We achieve low losses utilizing resist reflow, temperature cycled deposition, and etch optimization in our process flow. The temperature cycling allows us to overcome the nitride stress limit and deposit thick films, enabling the fabrica-

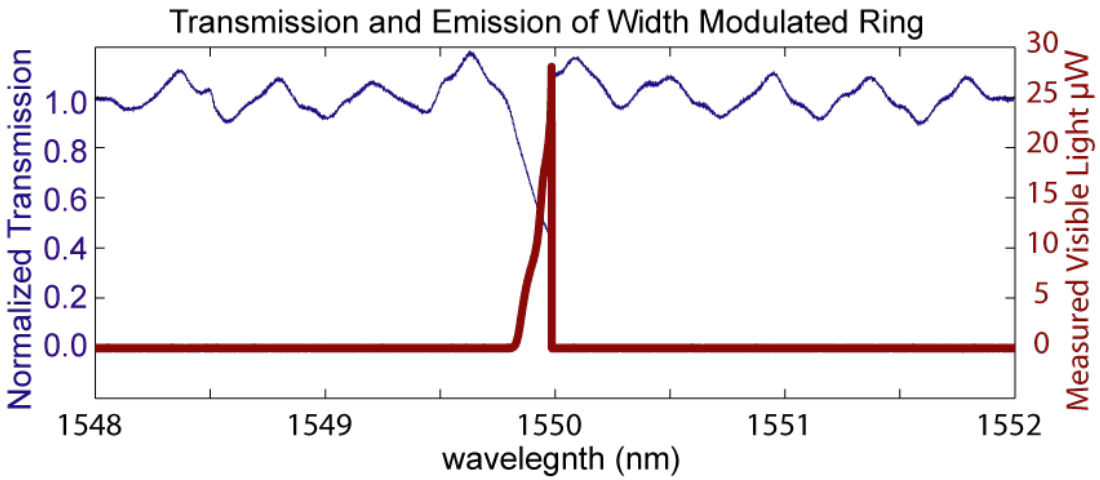

Figure 8.5: Normalized transmission and emission of waveguide coupled ring. The ring width modulation period is $\Lambda = 14.72$. The height of the ring is 740 nm. Emission is plotted as measured from the top.

tion of high confinement waveguides. The low loss and high confinement are applicable for low power, dense on chip integration.

CHAPTER 9

CONCLUSION AND OUTLOOK

The growth of integrated fabrication technology of micro and nanostructures has already benefited technology beyond microelectronics and is likely to continue. For example, vertical cavity surface emitting lasers, first shown in 1979, are now mass produced and widely used. The gains in efficiency of information transfer over waveguide structures will eventually force the use of photonics on smaller length scales in telecommunication industry. It is likely several improvements have to take place before commercial use of integrated silicon photonics is more prevalent. Packaging, one of the biggest obstacles would have to be overcome. Propagation losses and transparency in visible spectrum would also benefit. Silicon nitride could potentially assist in those aspects due to its already standard in microelectronic fabrication. Other uses which could benefit from nitride are life sciences. Sensing in visible range could benefit from silicon nitride integrated devices, with some interesting results already shown [].

APPENDIX A

LEDIT SCRIPTING

The layout and design of photonic chips is critical to efficient fabrication and testing of new device ideas and optical materials. The typical layout is composed of waveguides, rings, and various bends to allow efficiently coupling of light in and out of a chip. The design must be compact to minimize fabrication time and material use. Typically this phase requires careful manual positioning and modification of waveguides and bends to make sure waveguides do not cross or come in close proximity to each other. When waveguides or rings have one or more slots, or are surrounded by trenches to accommodate positive resists, this process can become extremely tedious and time consuming.

A popular layout tool, LEdit by TannerTools, allows user written functions in C to generate complex structures. A set of libraries was developed to simplify the process of creating photonic chips. Below we list a set of primary functions and structures with explanations how they are composed to create a typical photonic device.

A.1 Structures and Constants

All of the library functions use a handle to track the position and parameters of a waveguide being written. The handle is just an integer array (length 30).

```
#define SMS_DIRECTION 0
#define SMS_X 1
#define SMS_Y 2
#define SMS_NUM_GUIDES 3
```

```
#define SMS_GUIDE_THICK 4
#define SMS_SLOT_THICK 5

#define SMS_UP 1
#define SMS_RIGHT 2
#define SMS_DOWN 3
#define SMS_LEFT 4
#define UM 1000

int waveguide_handle[30];
```

LEdit uses nanometers as the global unit of length. The handle stores the following values,

```
waveguide_handle[SMS_DIRECTION]=SMS_UP | SMS_DOWN | SMS_LEFT | SMS_RIGHT;
```

This is the direction the waveguide is going, currently only four are directly supported.

```
waveguide_handle[SMS_X]
waveguide_handle[SMS_Y]
```

These are current coordinate of the waveguide handle position.

```
waveguide_handle[SMS_NUM_GUIDES]
```

This is the number of sections in a waveguide (normal waveguide has one section, single slot waveguide has two sections)

```
waveguide_handle[SMS_GUIDE_THICK + 2*n]
waveguide_handle[SMS_SLOT_THICK + 2*n]
```

These values describe the width of the waveguide section $n, (n = 0...SMS\_NUM\_GUIDES - 1)$, and the width of slot length adjacent to the guide.

After the last segment of the waveguide cross section, the void section is usually left as 0.

Example 1: 450 nm waveguide centered at the origin pointing in the positive y direction.

```
waveguide_handle[SMS_DIRECTION]=SMS_UP;
waveguide_handle[SMS_X]=0;
waveguide_handle[SMS_Y]=0;
waveguide_handle[SMS_NUM_GUIDES]=1;
waveguide_handle[SMS_GUIDE_THICK + 0]=450;
waveguide_handle[SMS_SLOT_THICK + 0]=0;
```

Example 2: 450 nm waveguide with a 50nm slot, centered at (0,1 mm) pointing in the positive x direction.

```
waveguide_handle[SMS_DIRECTION]=SMS_RIGHT;
waveguide_handle[SMS_X]=0;
waveguide_handle[SMS_Y]=1000*UM;
waveguide_handle[SMS_NUM_GUIDES]=2;
waveguide_handle[SMS_GUIDE_THICK + 0]=200;
waveguide_handle[SMS_SLOT_THICK + 0]=50;
waveguide_handle[SMS_GUIDE_THICK + 1]=200;
waveguide_handle[SMS_SLOT_THICK + 1]=0;
```

A.2 Functions

```
void goStraight(int slot[30],double distance,LLayer theLayer)
```

Writes a waveguide of length *distance* starting from the current handle position *slot*. The waveguide is written on the LEdit layer *theLayer*.

```
void goMStraight(int slot[30],int mark[30],int distance,int st,LLayer theLayer)
```

Like **goStraight**, writes a waveguide of length *distance* starting from the current handle position *slot*. The waveguide is written on the LEdit layer *theLayer*. Additionally write a 20 micron length line parallel to the waveguide, and 10 microns away, whenever the main waveguides crosses $n * st, n \in \mathbb{Z}$ absolute coordinate on either x or y axis. This is used to mark the field stitch positions of the E-beam tool. This allows the users to easily check for tool stitching. A typical pattern requires the E-beam to reposition the stage, this leads to misalignment between different field sections. The field size on a JEOL 9300 is 1 mm, and on the VB6 is 0.3 mm.

```
void  goTStraight(int slot[30],int taperto[30],double distance,LLayer theLayer)
```

Like **goStraight**, writes a waveguide of length *distance* starting from the current handle position *slot*. The waveguide is written on the LEdit layer *theLayer*. The cross section of the waveguide is linearly tapered between cross sections described by *slot* and *taperto*. The *taperto* cross section is copied to *slot* handle.

```
void goLeft(int slot[30],double distance,LLayer theLayer)
void goRight(int slot[30],double distance,LLayer theLayer)
```

Writes a 90 degree waveguide turn of radius *distance* starting from the current handle position *slot*. The waveguide is written on the LEdit layer. *theLayer*.

```
void number(int num, double xCoord, double yCoord,double sc)
```

Writes a number *num* at *(xCoord,yCoord)*. The waveguide is written on the LEdit layer. *theLayer*. The numbers are created as instances of cells '0'...'9', which must be predefined in the LEdit file. The *sc* is an integer scaling factor, the size of instanced sells is scaled $1/sc$.

A.3 SMS.H

```
/*
SMS.H
SLOT MANAGMENT SYSTEM
Alexander Gondarenko
*/
#define SMS_DIRECTION 0
#define SMS_X 1
#define SMS_Y 2
#define SMS_NUM_GUIDES 3
#define SMS_GUIDE_THICK 4
#define SMS_SLOT_THICK 5
#define SMS_UP 1
#define SMS_RIGHT 2
#define SMS_DOWN 3
#define SMS_LEFT 4
#define UM 1000

void goInst(int slot[30],char iname[30],int angl)
{
        LCell cell,instance_cell;
        LTransform_Ex99 transform;
        LPoint repeat_cnt,delta;
        LFile cfile;
        LMagnification mag;
        LRect iBox;
        LInstance iInst;
        LObject iObj;
        int i,dig1,r;
        char cname[10];
        mag.num=10;
        mag.num=10;
        //transform=LTransform_Set(0,0,0,mag);
        transform=LTransform_Zero();
        repeat_cnt.x=1;
        repeat_cnt.y=1;
        delta.x=0;
        delta.y=0;
        cell=LCell_GetVisible( );
        cfile= LCell_GetFile ( cell );
//      instance_cell = LCell_Find(cfile,"tape100");


//      LInstance_New(cell,instance_cell,transform,repeat_cnt,delta);



        delta.x=0;
        delta.y=0;
        transform.translation.x=slot[1];
        transform.translation.y=slot[2]+slot[4]/2;
        transform.magnification.num=1;
        transform.orientation=angl;
```

```
        instance_cell = LCell_Find(cfile,iname);

        iInst=LInstance_New_Ex99(cell,instance_cell,transform,repeat_cnt,delta);
        iBox=LInstance_GetMbb(iInst);
//      iBox=LCell_GetMbb(instance_cell);
         transform.translation.x=slot[1]+slot[1]-(iBox.x1+iBox.x0)/2-(iBox.x1-iBox.x0)
             /2;
        transform.translation.y=slot[2]+slot[2]-(iBox.y1+iBox.y0)/2+slot[4];

//      transform.orientation=45;
        LInstance_Set_Ex99(cell,iInst,transform,repeat_cnt,delta);
        slot[1]=slot[1]-(iBox.x1-iBox.x0);
}

void makeWheel(int slot[30],double rad,double spokew,LLayer theLayer){
        int spoke[30];

        spoke[0]=SMS_UP;
        spoke[1]=slot[1]+rad;
        spoke[2]=slot[2];
        spoke[3]=2;
        spoke[4]=0;
        spoke[5]=-spokew/2;
        spoke[6]=spokew;
        spoke[7]=0;

        goRight(slot,rad,theLayer);goRight(slot,rad,theLayer);
        goRight(slot,rad,theLayer);goRight(slot,rad,theLayer);

        goStraight(spoke,rad-slot[4]+50,theLayer);
        spoke[0]=SMS_RIGHT;spoke[1]=slot[1]+rad;spoke[2]=slot[2];
        goStraight(spoke,rad-slot[4]+50,theLayer);
        spoke[0]=SMS_LEFT;spoke[1]=slot[1]+rad;spoke[2]=slot[2];
        goStraight(spoke,rad-slot[4]+50,theLayer);
        spoke[0]=SMS_DOWN;spoke[1]=slot[1]+rad;spoke[2]=slot[2];
        goStraight(spoke,rad-slot[4]+50,theLayer);
}

void makeRing(int slot[30],int thering[30],double rad,double space,double space2,
    LLayer theLayer){
        int i,j;
        double sx,sy,tx,ty,tw,sx0,sy0;
        double cx,cy,distance;
        char                    dummy1[30];
        char        tlname[30];
        LCell       Cell_Draw   = LCell_GetVisible( );
        LFile       File_Draw   = LCell_GetFile ( Cell_Draw );
        LPoint      guide[10];
        LPoint      bbox[4];
        LObject     trench[3],disk[2],prevO;
        LCoord      am;
        LLayer      tempLayer;
        LTorusParams    tParams;

        LLayer_New(File_Draw,theLayer,"tl_sms");
```

```
        tempLayer=LLayer_Find(File_Draw,"tl_sms");
        slot[29]=slot[29]+distance;
        sx=0;
        sy=0;
        tw=slot[(slot[SMS_NUM_GUIDES]-1)*2+SMS_GUIDE_THICK];//outer trench width
        distance=(rad+tw)*2;
        if(slot[SMS_DIRECTION] == SMS_UP)    {/* I be going up */   cx=0;cy=1;tx=1;ty
            =0;}
        if(slot[SMS_DIRECTION] == SMS_RIGHT){/* I be going right */cx=1;cy=0;tx=0;ty
            =-1;}
        if(slot[SMS_DIRECTION] == SMS_DOWN) {/* I be going down */ cx=0;cy=-1;tx=-1;ty
            =0;}
        if(slot[SMS_DIRECTION] == SMS_LEFT) {/* I be going left */ cx=-1;cy=0;tx=0;ty
            =1;}
//main bus
            for(i=0;i<slot[SMS_NUM_GUIDES];i++){
                guide[0].x=slot[SMS_X]+sx;
                guide[0].y=slot[SMS_Y]+sy;
                guide[1].x=slot[SMS_X]+cx*distance+sx;
                guide[1].y=slot[SMS_Y]+cy*distance+sy;
                guide[2].x=slot[SMS_X]+sx+cx*distance+tx*slot[SMS_GUIDE_THICK
                    +2*i];
                guide[2].y=slot[SMS_Y]+sy+cy*distance+ty*slot[SMS_GUIDE_THICK
                    +2*i];
                guide[3].x=slot[SMS_X]+sx+tx*slot[SMS_GUIDE_THICK+2*i];
                guide[3].y=slot[SMS_Y]+sy+ty*slot[SMS_GUIDE_THICK+2*i];
                prevO=trench[0];
                trench[0]=LPolygon_New(Cell_Draw, theLayer,guide, 4);
                sx=sx+tx*slot[SMS_GUIDE_THICK+2*i]+tx*slot[SMS_SLOT_THICK+2*i];
                    //shift to next rail
                sy=sy+ty*slot[SMS_GUIDE_THICK+2*i]+ty*slot[SMS_SLOT_THICK+2*i];
                    //shift to next rail
            }
//drop bus
            sx0=sx;sy0=sy;
            sx=sx+tx*(rad*2+space+space2-2*slot[SMS_GUIDE_THICK]); //shift to next
                rail
            sy=sy+ty*(rad*2+space+space2-2*slot[SMS_GUIDE_THICK]); //shift to next
                rail

            for(i=0;i<slot[SMS_NUM_GUIDES];i++){
                guide[0].x=slot[SMS_X]+sx;
                guide[0].y=slot[SMS_Y]+sy;
                guide[1].x=slot[SMS_X]+cx*distance+sx;
                guide[1].y=slot[SMS_Y]+cy*distance+sy;
                guide[2].x=slot[SMS_X]+sx+cx*distance+tx*slot[SMS_GUIDE_THICK
                    +2*i];
                guide[2].y=slot[SMS_Y]+sy+cy*distance+ty*slot[SMS_GUIDE_THICK
                    +2*i];
                guide[3].x=slot[SMS_X]+sx+tx*slot[SMS_GUIDE_THICK+2*i];
                guide[3].y=slot[SMS_Y]+sy+ty*slot[SMS_GUIDE_THICK+2*i];
                prevO=trench[0];
                if(i==0){
                    trench[2]=LPolygon_New(Cell_Draw, theLayer,guide, 4);
                }else{
```

```
                LPolygon_New(Cell_Draw, theLayer,guide, 4);
        }
        sx=sx+tx*slot[SMS_GUIDE_THICK+2*i]+tx*slot[SMS_SLOT_THICK+2*i];
              //shift to next rail
        sy=sy+ty*slot[SMS_GUIDE_THICK+2*i]+ty*slot[SMS_SLOT_THICK+2*i];
              //shift to next rail
}

i=slot[SMS_NUM_GUIDES]-1;
sx=sx0;sy=sy0;
sx=sx-tx*slot[SMS_GUIDE_THICK+2*i]-tx*slot[SMS_SLOT_THICK+2*i]; //shift
     to next rail
sy=sy-ty*slot[SMS_GUIDE_THICK+2*i]-ty*slot[SMS_SLOT_THICK+2*i]; //shift
     to next rail

bbox[0].x=slot[SMS_X]+sx;
bbox[0].y=slot[SMS_Y]+sy;
bbox[1].x=slot[SMS_X]+cx*distance+sx;
bbox[1].y=slot[SMS_Y]+cy*distance+sy;
 bbox[2].x=slot[SMS_X]+sx+cx*distance+tx*(0*slot[SMS_GUIDE_THICK+2*i]+
     rad*2-0*tw+space2+space);
 bbox[2].y=slot[SMS_Y]+sy+cy*distance+ty*(0*slot[SMS_GUIDE_THICK+2*i]+
     rad*2-0*tw+space2+space);
 bbox[3].x=slot[SMS_X]+sx+tx*(0*slot[SMS_GUIDE_THICK+2*i]+rad*2-0*tw+
     space2+space);
 bbox[3].y=slot[SMS_Y]+sy+ty*(0*slot[SMS_GUIDE_THICK+2*i]+rad*2-0*tw+
     space2+space);

guide[0].x=slot[SMS_X];
guide[0].y=slot[SMS_Y]+rad+tw;
for(i=0;i<slot[SMS_NUM_GUIDES]-1;i++){
          guide[0].x=guide[0].x+slot[SMS_GUIDE_THICK+2*i]+slot[
              SMS_SLOT_THICK+2*i];
}

guide[0].x=guide[0].x+rad+space;
trench[1]=LCircle_New(Cell_Draw,theLayer,guide[0],rad+tw);
disk[0]=LPolygon_New(Cell_Draw,theLayer,bbox,4);
am=0;
 LCell_BooleanOperation(Cell_Draw,LBoolOp_AND,am,trench,3,disk,1,
     tempLayer,LTRUE);
trench[0]=LObject_GetList(Cell_Draw,tempLayer);
j=0;
for(i=thering[SMS_NUM_GUIDES]-2;i>=0;i--){
        tParams.dStartAngle=0;
        tParams.dStopAngle=0;
        tParams.ptCenter.x = guide[0].x;
        tParams.ptCenter.y = guide[0].y;
        tParams.nOuterRadius = rad;
        tParams.nInnerRadius = rad - thering[SMS_SLOT_THICK+2*i];
        disk[j] = LTorus_CreateNew(Cell_Draw, theLayer,&tParams);
        rad=rad-thering[SMS_SLOT_THICK+2*i]-thering[SMS_GUIDE_THICK+2*i
            ];
        j++;
}
```

```
                //tlname='tl';

                //LObject_Delete(Cell_Draw,disk[0]);

                 LCell_BooleanOperation(Cell_Draw,LBoolOp_XOR,am,trench,1,disk,j,
                     theLayer,LTRUE);
                slot[SMS_X]=slot[SMS_X]+cx*distance;
                slot[SMS_Y]=slot[SMS_Y]+cy*distance;
                LLayer_Delete(File_Draw,tempLayer);
}


void  goStraight(int slot[30],double distance,LLayer theLayer){
        int i;
        double sx,sy,tx,ty;
        double cx,cy;
        char                    dummy1[30];
        LCell       Cell_Draw   = LCell_GetVisible( );
        LFile       File_Draw   = LCell_GetFile ( Cell_Draw );
        LPoint      guide[10];
        slot[29]=slot[29]+distance;
        sx=0;
        sy=0;

        if(slot[SMS_DIRECTION] == SMS_UP)   {/* I be going up */   cx=0;cy=1;tx=1;ty
            =0;}
        if(slot[SMS_DIRECTION] == SMS_RIGHT){/* I be going right */cx=1;cy=0;tx=0;ty
            =-1;}
        if(slot[SMS_DIRECTION] == SMS_DOWN) {/* I be going down */ cx=0;cy=-1;tx=-1;ty
            =0;}
        if(slot[SMS_DIRECTION] == SMS_LEFT) {/* I be going left */ cx=-1;cy=0;tx=0;ty
            =1;}

            for(i=0;i<slot[SMS_NUM_GUIDES];i++){
                    guide[0].x=slot[SMS_X]+sx;
                    guide[0].y=slot[SMS_Y]+sy;
                    guide[1].x=slot[SMS_X]+cx*distance+sx;
                    guide[1].y=slot[SMS_Y]+cy*distance+sy;
                    guide[2].x=slot[SMS_X]+sx+cx*distance+tx*slot[SMS_GUIDE_THICK
                        +2*i];
                    guide[2].y=slot[SMS_Y]+sy+cy*distance+ty*slot[SMS_GUIDE_THICK
                        +2*i];
                    guide[3].x=slot[SMS_X]+sx+tx*slot[SMS_GUIDE_THICK+2*i];
                    guide[3].y=slot[SMS_Y]+sy+ty*slot[SMS_GUIDE_THICK+2*i];

                    LPolygon_New(Cell_Draw, theLayer,guide, 4);
                    sx=sx+tx*slot[SMS_GUIDE_THICK+2*i]+tx*slot[SMS_SLOT_THICK+2*i];
                          //shift to next rail
                    sy=sy+ty*slot[SMS_GUIDE_THICK+2*i]+ty*slot[SMS_SLOT_THICK+2*i];
                          //shift to next rail
            }
            slot[SMS_X]=slot[SMS_X]+cx*distance;
            slot[SMS_Y]=slot[SMS_Y]+cy*distance;
      /* No more going */
```

```
}

void  goMStraight(int slot[30],int mark[30],int distance,int st,LLayer theLayer){
        if(slot[SMS_DIRECTION] == SMS_UP){
                if(st-slot[2]%st <distance){
                        mark[1]=slot[1]-10*UM;
                        mark[2]=slot[2]+st-slot[2]%st-10*UM;
                        mark[0]=slot[0];
                        mark[4]=1000;
                        goStraight(mark,5*UM,theLayer);
                        mark[3]=2;mark[4]=100;mark[5]=0;mark[6]=0;mark[7]=0;
                        goStraight(mark,4900,theLayer);
                        mark[3]=2;mark[4]=100;mark[5]=200;mark[6]=200;mark[7]=0;
                        goStraight(mark,200,theLayer);
                        mark[3]=1;mark[4]=100;mark[5]=200;mark[6]=200;mark[7]=0;
                        goStraight(mark,4900,theLayer);
                        mark[4]=1000;
                        goStraight(mark,5*UM,theLayer);
                        if(distance > st){
                                goStraight(slot,st,theLayer);
                                goMStraight(slot,mark,distance-st,st,theLayer);
                        }else{
                                goStraight(slot,distance,theLayer);
                        }               }else{
                        goStraight(slot,distance,theLayer);
                }
        }

        if(slot[SMS_DIRECTION] == SMS_DOWN){
                if(slot[2]%st <distance){
                        mark[1]=slot[1]-10*UM;
                        mark[2]=slot[2]-slot[2]%st+10*UM;
                        mark[0]=slot[0];
                        mark[4]=1000;
                        goStraight(mark,5*UM,theLayer);
                        mark[4]=100;
                        goStraight(mark,10*UM,theLayer);
                        mark[4]=1000;
                        goStraight(mark,5*UM,theLayer);
                        if(distance > st){
                                goStraight(slot,st,theLayer);
                                goMStraight(slot,mark,distance-st,st,theLayer);
                        }else{
                                goStraight(slot,distance,theLayer);
                        }               }else{
                        goStraight(slot,distance,theLayer);
                }
        }

        if(slot[SMS_DIRECTION] == SMS_LEFT){
                if(slot[1]%st <distance){
                        mark[1]=slot[1]-slot[1]%st+10*UM;
                        mark[2]=slot[2]-10*UM;
                        mark[0]=slot[0];
                        mark[4]=1000;
```

```
                        goStraight(mark,5*UM,theLayer);
                        mark[4]=100;
                        goStraight(mark,10*UM,theLayer);
                        mark[4]=1000;
                        goStraight(mark,5*UM,theLayer);
                        if(distance > st){
                                goStraight(slot,st,theLayer);
                                goMStraight(slot,mark,distance-st,st,theLayer);
                        }else{
                                goStraight(slot,distance,theLayer);
                        }               }else{
                        goStraight(slot,distance,theLayer);
                }
        }

        if(slot[SMS_DIRECTION] == SMS_RIGHT){
                if(st-slot[1]%st <distance){
                        mark[1]=slot[1]+st-slot[1]%st-10*UM;
                        mark[2]=slot[2]-10*UM;
                        mark[0]=slot[0];
                        mark[4]=1000;
                        goStraight(mark,5*UM,theLayer);
                        mark[4]=100;
                        goStraight(mark,10*UM,theLayer);
                        mark[4]=1000;
                        goStraight(mark,5*UM,theLayer);
                        if(distance > st){
                                goStraight(slot,st,theLayer);
                                goMStraight(slot,mark,distance-st,st,theLayer);
                        }else{
                                goStraight(slot,distance,theLayer);
                        }
                }else{
                        goStraight(slot,distance,theLayer);
                }
        }

}

void  goTStraight(int slot[30],int taperto[30],double distance,LLayer theLayer){
        int i;
        double sx,sy,tx,ty;
        double cx,cy,w,w2,dw;
        char                    dummy1[30];
        LCell       Cell_Draw   = LCell_GetVisible( );
        LFile       File_Draw   = LCell_GetFile ( Cell_Draw );
        LPoint      guide[10];
        slot[29]=slot[29]+distance;
        sx=0;
        sy=0;

        if(slot[SMS_DIRECTION] == SMS_UP)   {/* I be going up */   cx=0;cy=1;tx=1;ty
            =0;}
        if(slot[SMS_DIRECTION] == SMS_RIGHT){/* I be going right */cx=1;cy=0;tx=0;ty
            =-1;}
```

```
        if(slot[SMS_DIRECTION] == SMS_DOWN) {/* I be going down */ cx=0;cy=-1;tx=-1;ty
            =0;}
        if(slot[SMS_DIRECTION] == SMS_LEFT) {/* I be going left */ cx=-1;cy=0;tx=0;ty
            =1;}

        w=0;
        for(i=0;i<slot[SMS_NUM_GUIDES];i++){
                w=w+slot[SMS_GUIDE_THICK+2*i];
                w=w+slot[SMS_SLOT_THICK+2*i];
        }//compute starting width of waveguide

        w2=0;
        for(i=0;i<taperto[SMS_NUM_GUIDES];i++){
                w2=w2+taperto[SMS_GUIDE_THICK+2*i];
                w2=w2+taperto[SMS_SLOT_THICK+2*i];
        }//compute ending width of waveguide
        dw=-(w2-w)/2;//shift in guide position to prevent sideways shift
        for(i=0;i<slot[SMS_NUM_GUIDES];i++){
                        guide[0].x=slot[SMS_X]+sx;
                        guide[0].y=slot[SMS_Y]+sy;

                        guide[1].x=slot[SMS_X]+cx*distance+sx+tx*dw;
                        guide[1].y=slot[SMS_Y]+cy*distance+sy+ty*dw;
                         guide[2].x=slot[SMS_X]+sx+cx*distance+tx*taperto[
                             SMS_GUIDE_THICK+2*i]+tx*dw;
                         guide[2].y=slot[SMS_Y]+sy+cy*distance+ty*taperto[
                             SMS_GUIDE_THICK+2*i]+ty*dw;

                        guide[3].x=slot[SMS_X]+sx+tx*slot[SMS_GUIDE_THICK+2*i];
                        guide[3].y=slot[SMS_Y]+sy+ty*slot[SMS_GUIDE_THICK+2*i];

                        LPolygon_New(Cell_Draw, theLayer,guide, 4);

                        dw=dw+taperto[SMS_GUIDE_THICK+2*i]+taperto[SMS_SLOT_THICK+2*i];
                        dw=dw-slot[SMS_GUIDE_THICK+2*i]-slot[SMS_SLOT_THICK+2*i];
                        sx=sx+tx*slot[SMS_GUIDE_THICK+2*i]+tx*slot[SMS_SLOT_THICK+2*i];
                              //shift to next rail
                        sy=sy+ty*slot[SMS_GUIDE_THICK+2*i]+ty*slot[SMS_SLOT_THICK+2*i];
                              //shift to next rail
                }
                slot[SMS_X]=slot[SMS_X]+cx*distance-tx*(w2-w)/2;
                slot[SMS_Y]=slot[SMS_Y]+cy*distance-ty*(w2-w)/2;

        for(i=0;i<taperto[SMS_NUM_GUIDES];i++){
                slot[SMS_GUIDE_THICK+2*i]=taperto[SMS_GUIDE_THICK+2*i];
                slot[SMS_SLOT_THICK+2*i] =taperto[SMS_SLOT_THICK+2*i];
        }//change the waveguide geometry to the one we tapered to

          /* No more going */

}

void goRight(int slot[30],double distance,LLayer theLayer){
        int i;
        double sx,sy,cx,cy,tx,ty;
```

```
        char                    dummy1[30];
        LCell       Cell_Draw   = LCell_GetVisible( );
        LFile       File_Draw   = LCell_GetFile ( Cell_Draw );
        LPoint      guide[10];
        LTorusParams    tParams;
        LObject         myTorus;
        slot[29]=slot[29]+distance*1.5708;
        sx=0;
        sy=0;

        switch(slot[SMS_DIRECTION]){
                case SMS_UP:
                tParams.dStartAngle=90;
                tParams.dStopAngle=180;
                cx=1;cy=0;tx=1;ty=1;
                slot[SMS_DIRECTION]=SMS_RIGHT;
                break;
                case SMS_RIGHT:
                tParams.dStartAngle=0;
                tParams.dStopAngle=90;
                cx=0;cy=-1;tx=1;ty=-1;
                slot[SMS_DIRECTION]=SMS_DOWN;
                break;
                case SMS_DOWN:
                tParams.dStartAngle=270;
                tParams.dStopAngle=360;
                cx=-1;cy=0;tx=-1;ty=-1;
                slot[SMS_DIRECTION]=SMS_LEFT;
           break;
           case SMS_LEFT:
                tParams.dStartAngle=180;
                tParams.dStopAngle=270;
                cx=0;cy=1;tx=-1;ty=1;
                slot[SMS_DIRECTION]=SMS_UP;
        }
                tParams.ptCenter.x = slot[SMS_X] + cx*distance;
                tParams.ptCenter.y = slot[SMS_Y] + cy*distance;
                for(i=0;i<slot[SMS_NUM_GUIDES];i++){
                        tParams.nOuterRadius = distance - sx - sy;
                        tParams.nInnerRadius = distance - sx - sy - slot[
                            SMS_GUIDE_THICK+2*i];
                        myTorus = LTorus_CreateNew(Cell_Draw, theLayer,&tParams);
                         sx=sx+cx*cx*slot[SMS_GUIDE_THICK+2*i]+cx*cx*slot[
                              SMS_SLOT_THICK+2*i];
                         sy=sy+cy*cy*slot[SMS_GUIDE_THICK+2*i]+cy*cy*slot[
                              SMS_SLOT_THICK+2*i];
                }

                slot[SMS_X]=slot[SMS_X]+tx*distance;
                slot[SMS_Y]=slot[SMS_Y]+ty*distance;

}
void goLeft(int slot[30],double distance,LLayer theLayer){
        int i;
        double sx,sy,cx,cy,tx,ty,tw;
```

```
char                    dummy1[30];
LCell       Cell_Draw   = LCell_GetVisible( );
LFile       File_Draw   = LCell_GetFile ( Cell_Draw );
LPoint      guide[10];
LTorusParams    tParams;
LObject         myTorus;
slot[29]=slot[29]+distance*1.5708;
sx=0;
sy=0;
tw=0;

for(i=0;i<slot[SMS_NUM_GUIDES];i++){
        tw=tw+slot[SMS_GUIDE_THICK+2*i];
        tw=tw+slot[SMS_SLOT_THICK+2*i];
}

switch(slot[SMS_DIRECTION]){
        case SMS_UP:
        tParams.dStartAngle=0;
        tParams.dStopAngle=90;
        cx=-1;cy=0;tx=-1;ty=1;
        slot[SMS_DIRECTION]=SMS_LEFT;
        break;
        case SMS_RIGHT:
        tParams.dStartAngle=270;
        tParams.dStopAngle=360;
        cx=0;cy=1;tx=1;ty=1;
        slot[SMS_DIRECTION]=SMS_UP;
        break;
        case SMS_DOWN:
        tParams.dStartAngle=180;
        tParams.dStopAngle=270;
        cx=1;cy=0;tx=1;ty=-1;
        slot[SMS_DIRECTION]=SMS_RIGHT;
    break;
    case SMS_LEFT:
        tParams.dStartAngle=90;
        tParams.dStopAngle=180;
        cx=0;cy=-1;tx=-1;ty=-1;
        slot[SMS_DIRECTION]=SMS_DOWN;
}
        tParams.ptCenter.x = slot[SMS_X] + cx*(distance-2*tw/4);
        tParams.ptCenter.y = slot[SMS_Y] + cy*(distance-2*tw/4);
        for(i=0;i<slot[SMS_NUM_GUIDES];i++){
                tParams.nInnerRadius = (distance - 2*tw/4) + sx + sy;
                tParams.nOuterRadius = (distance - 2*tw/4) + sx + sy + slot[
                    SMS_GUIDE_THICK+2*i];
                myTorus = LTorus_CreateNew(Cell_Draw, theLayer,&tParams);
                 sx=sx+cx*cx*slot[SMS_GUIDE_THICK+2*i]+cx*cx*slot[
                     SMS_SLOT_THICK+2*i];
                 sy=sy+cy*cy*slot[SMS_GUIDE_THICK+2*i]+cy*cy*slot[
                     SMS_SLOT_THICK+2*i];
        }

        slot[SMS_X]=slot[SMS_X]+tx*(distance-2*tw/4);
```

```
                slot[SMS_Y]=slot[SMS_Y]+ty*(distance-2*tw/4);
}

//there best be blank line at the ends of a file, otherwise
//the script interpreter freaks out
```

A.4 NUMBERS2.H

```
/* Number Functions                    */
/* Feb 26 2007                         */


void number(int num, double xCoord, double yCoord,double sc)
{
        LCell cell,instance_cell;
        LTransform transform;
        LPoint repeat_cnt,delta;
        LFile cfile;
        LMagnification mag;
        int i,dig1,r;
        char cname[10];
        mag.num=10;
        mag.num=10;
        //transform=LTransform_Set(0,0,0,mag);
        transform=LTransform_Zero();
        repeat_cnt.x=1;
        repeat_cnt.y=1;
        delta.x=0;
        delta.y=0;
        cell=LCell_GetVisible( );
        cfile= LCell_GetFile ( cell );
//      instance_cell = LCell_Find(cfile,"tape100");


//      LInstance_New(cell,instance_cell,transform,repeat_cnt,delta);

        while(num>0){
        dig1=num%10;
        delta.x=0;
        delta.y=0;
        transform.translation.x=xCoord;
        transform.translation.y=yCoord;
        transform.magnification.num=sc;
        r=rand()%20-10;
//      transform.orientation=r+360;
        r=rand()%20-10;
        itoa(dig1,cname,10);
        instance_cell = LCell_Find(cfile,cname);
        LInstance_New(cell,instance_cell,transform,repeat_cnt,delta);
        num=num/10;
        xCoord=xCoord - 12000*transform.magnification.num;
        }
}
```

```
void numberv(int num, double xCoord, double yCoord,double sc)
{
        LCell cell,instance_cell;
        LTransform transform;
        LPoint repeat_cnt,delta;
        LFile cfile;
        LMagnification  mag;
        int i,dig1,r;
        char cname[10];
        mag.num=10;
        mag.num=10;
        //transform=LTransform_Set(0,0,0,mag);
        transform=LTransform_Zero();
        repeat_cnt.x=1;
        repeat_cnt.y=1;
        delta.x=0;
        delta.y=0;
        cell=LCell_GetVisible( );
        cfile= LCell_GetFile ( cell );
//      instance_cell = LCell_Find(cfile,"tape100");


//      LInstance_New(cell,instance_cell,transform,repeat_cnt,delta);

        while(num>0){
        dig1=num%10;
        delta.x=0;
        delta.y=0;
        transform.translation.x=xCoord;
        transform.translation.y=yCoord;
        transform.magnification.num=sc;
        r=rand()%20-10;
   transform.orientation=90;
        r=rand()%20-10;
        itoa(dig1,cname,10);
        instance_cell = LCell_Find(cfile,cname);
        LInstance_New(cell,instance_cell,transform,repeat_cnt,delta);
        num=num/10;
        yCoord=yCoord - 12000*transform.magnification.num;
        }
}
```

A.5 RINGS.C

```
//*****************************************************************//
//  Script to generate a set of rings coupled to waveguides
//
//  Alexander Gondarenko, 2009, August
//*****************************************************************//
module nanotapers_module{
#include "ldata.h"
#include <stdlib.h>
```

```
#include <math.h>
#include <string.h>
#include <stdio.h>
#include "lcomp.h"
#include "sms.h"
#include "numbers2.h"

void draw_polish_marks(int guide[30],LLayer theLayer){
        LLayer      tempLayer;
        LCell       Cell_Draw   = LCell_GetVisible( );
        LFile       File_Draw   = LCell_GetFile ( Cell_Draw );
        int temp[30],mark[30],t2;

        //make temp layer
        LLayer_New(File_Draw,theLayer,"temp_sms");
        tempLayer=LLayer_Find(File_Draw,"temp_sms");


        copyHandle(temp,guide);
        temp[3]=1;temp[4]=1000;temp[5]=0;
        for(t2=0;t2<=10;t2++){
                copyHandle(mark,temp);
                goStraight(mark,temp[4],tempLayer);
                mark[0]=mark[0]%4+1;
                goStraight(mark,20*UM,tempLayer);//LObject_Delete(Cell_Draw,
                     LObject_GetList(Cell_Draw,tempLayer));
                goStraight(mark,4*UM+(t2%2)*4*UM,theLayer);

                copyHandle(mark,temp);
                mark[0]=(mark[0]+2)%4+1;
                goStraight(mark,20*UM,tempLayer);//LObject_Delete(Cell_Draw,
                     LObject_GetList(Cell_Draw,tempLayer));
                goStraight(mark,2*UM+(t2%4==3)*6*UM,theLayer);

                 goStraight(temp,25*UM,tempLayer);//LObject_Delete(Cell_Draw,
                      LObject_GetList(Cell_Draw,tempLayer));
        }

        //delete temp layer
        LLayer_Delete(File_Draw,tempLayer);
}

void  waveguides_Macro ( void )
{
        char                    LayerNameAndNumber[30];
        char                    LayerNumber[30];
        char                    tempLayerName[30];
        char                    dummy1[30];
        int         add_drop[30],slot[30],ring[30],taper[30],anchor[30],guide[30],
            stitch[30],wgWriting,wgSpacing,duplicates,ngd,offsetInOut,bRad,offset,
            pspace,turn,turns;
        int         of,of1,of2;//offsets to hit the write cells
        int         t1,t2,t3,flds,gap;//track length
        int         vp,tc;//variable path, taper calibration
        int                     ring_separation,ring_guide_width;
```

```
    int          tool;//0 JEOL
                                                //1 VB

    float PerL,PerD,wgW,pi2;
    int   PerN;

    int rad;
    LTorusParams     tParams;
    LObject          myTorus;
    LRenderingAttribute     ra;
    LStipple fillPattern = {0xFF, 0xFF, 0xFF, 0xFF, 0xFF, 0xFF, 0xFF, 0xFF}; /*
        Pattern */
    LCell        Cell_Draw   = LCell_GetVisible( );
    LFile        File_Draw   = LCell_GetFile ( Cell_Draw );
    LLayer           Layer_Draw  = LLayer_GetCurrent ( File_Draw );

    wgSpacing=50*UM; //waveguide spacing (standard)
    pi2=3.14159*2.;

    bRad=50*UM; //bend radius
    duplicates=10; //number of guides
    offset=3000*UM; //input to output offset to the left (3mm)
    of=-45*UM-1*wgSpacing+3000*UM;

    tool=0;// 0 JEOL, 1 VB6

    wgW=1600;
// INITIALIZE field size according to the tool
    if(tool==0){//JEOL
            flds=1000*UM;
    }else{//VB6
            flds=300*UM;
    }


    /
    //BELOW IS A TYPICAL HANDLE DESCRIPTIOR
    taper[0]=SMS_UP;//INITIAL DIRECTION WHERE GUIDE POINTS
    taper[SMS_X]=0;      //X coordinate
    taper[SMS_Y]=0;    //Y coordinate
    taper[SMS_NUM_GUIDES]=1; //Number of sections to guide (normal guide has 1,
        slot guide has 2...)
    taper[4]=300;                    //Width of 1st section
    taper[5]=0;                              //Width of space after first section

    //SETUP
//define predefined handles for various parts of waveguide (taper, etc..)
    stitch[0]=SMS_UP;stitch[1]=0;stitch[2]=0;stitch[3]=1;
stitch[4]=200;stitch[5]=0;

    anchor[0]=SMS_UP;anchor[1]=0;anchor[2]=0;anchor[3]=1;
    anchor[4]=3000;anchor[5]=0;

    guide[0]=SMS_UP;guide[1]=0;guide[2]=0;guide[3]=1;
    guide[4]=1000;guide[5]=0;
```

```
ring[0]=SMS_UP; ring[1]=0; ring[2]=5*UM-000*UM; ring[3]=1;
ring[4]=.1*UM; ring[5]=0;

//waveguide LOOP
//this makes the different guides on each die
for(ngd=0;ngd<duplicates;ngd++){
        //waveguide spacing
        wgSpacing=50*UM;


        //initialize main bus position and parameters...
        slot[0]=SMS_UP; //up is positive y direction

        slot[SMS_X]=offset+wgSpacing;//X starting position
        offset=slot[1]; of=slot[1];


        slot[SMS_UP]=0*UM;                  //Y starting position
        slot[SMS_NUM_GUIDES]=1;             //simple 1 section waveguide
        slot[SMS_GUIDE_THICK]=anchor[4];    //width of waveguide
        slot[SMS_SLOT_THICK]=0;             //space after rail

        slot[29]=0;


        goStraight(slot,3*UM,Layer_Draw);//make anchor
        goTStraight(slot,taper,3*UM,Layer_Draw);//transition to tapered width
        goStraight(slot,50*UM,Layer_Draw);//make coupling taper

        draw_polish_marks(slot,Layer_Draw);

        goTStraight(slot,guide,250*UM,Layer_Draw);//tapering region
        numberv(ngd+1,slot[SMS_X]+20*UM,slot[SMS_Y]+70*UM,1);//write # of guide

        //make waveguide before the rings
        if(tool==0){//JEOL
                goStraight(slot,1000*UM-slot[2],Layer_Draw);
        }else{//VB
                goStraight(slot,(flds*2)-slot[2]+50*UM,Layer_Draw);
        }
        guide[4]=800;
        //taper down the guide to enhance coupling to ring
        goTStraight(slot,guide,100*UM,Layer_Draw);
        goStraight(slot,50*UM,Layer_Draw);
        copyHandle(ring,slot); //copies entire handle
        copyCSection(ring,slot); //copies just the cross section description

        ring[SMS_GUIDE]=wgW;

//offset the ring position with respect to the waveguide
//the space between ring and slot is ngd*10 nanometers
        ring[1]=ring[1]+slot[4]+ngd*10;
```

```
        //
        // WRITE THE RING
        // make ring by writing 4 right turns
        //
                goRight(ring,5*UM,Layer_Draw);goRight(ring,5*UM,Layer_Draw);
        goRight(ring,5*UM,Layer_Draw);goRight(ring,5*UM,Layer_Draw);

        // Write the ring to waveguide space next to the ring
                numberv(ngd*10,slot[SMS_X]+20*UM,slot[SMS_Y]-70*UM,2);


                goStraight(slot,50*UM,Layer_Draw);
                guide[4]=1000;//reset waveguide width to micron
                //taper out to waveguide size
                goTStraight(slot,guide,100*UM,Layer_Draw);

                //turn the waveguide to offset the output
                goLeft(slot,wgSpacing,Layer_Draw);
                goRight(slot,wgSpacing,Layer_Draw);

                ////////////////////////////
                // Writes the rest of main bus guide after the rings
                ////////////////////////////

                goStraight(slot,rad+bRad+100*UM,Layer_Draw);

                if(tool==0){//JEOL
                        goMStraight(slot,stitch,2000*UM-306*UM-slot[2],flds,Layer_Draw)
                            ;
                }else{//VB6
                        goMStraight(slot,stitch,4200*UM-306*UM-slot[2],flds,Layer_Draw)
                            ;
                }

                //taper down to coupling region

                draw_polish_marks(slot,Layer_Draw);
                goTStraight(slot,taper,250*UM,Layer_Draw);
                //label the guide
                number(ngd+1,slot[SMS_X]+30*UM,slot[SMS_Y]-300*UM,1);

                goMStraight(slot,stitch,50*UM,flds,Layer_Draw);//narrow part of taper
                goTStraight(slot,anchor,3*UM,Layer_Draw);//transition to making anchor
                goStraight(slot,3*UM,Layer_Draw);//make anchor


        }
        }
        delete_temp_layer();

}

//**********************************//
//********** Macro Register **********//
//**********************************//
```

```
void  nanotapers_macro_register ( void )
{
        //LMacro_Register("bowtie", "BowtieMacro");
        LMacro_BindToHotKey ( KEY_F10, "waveguides", "waveguides_Macro" );
}
}/* End of Module */
nanotapers_macro_register();
```

BIBLIOGRAPHY

[1] I. H Agha, Y. Okawachi, M. A Foster, J. E Sharping, and A. L Gaeta. Four-wave-mixing parametric oscillations in dispersion-compensated high-Q silica microspheres. *Physical Review A*, 76(4):43837, 2007.

[2] Y. Akahane, T. Asano, B. S Song, and S. Noda. Fine-tuned high-Q photonic-crystal nanocavity. *Optics Express*, 13(4):12021214, 2005.

[3] Vilson R. Almeida, Carlos A. Barrios, Roberto R. Panepucci, and Michal Lipson. All-optical control of light on a silicon chip. *Nature*, 431(7012):1081–1084, October 2004.

[4] Vilson R. Almeida, Roberto R. Panepucci, and Michal Lipson. Nanotaper for compact mode conversion. *Optics Letters*, 28(15):1302–1304, 2003.

[5] T. W. Ang, G. T. Reed, A. Vonsovici, A. G. R. Evans, P. R. Routley, and M. R. Josey. Effects of grating heights on highly efficient unibond SOIwaveguide grating couplers. *IEEE Photonics Technology Letters*, 12(1):5961, 2000.

[6] T. W. Ang, G. T. Reed, A. Vonsovici, A. G. R. Evans, P. R. Routley, and M. R. Josey. Highly efficient unibond silicon-on-insulator blazed grating couplers. *Applied Physics Letters*, 77(25):4214–4216, December 2000.

[7] C. A. Barrios, B. Sanchez, K. B. Gylfason, A. Griol, H. Sohlstr?m, M. Holgado, and R. Casquel. Demonstration of slot-waveguide structures on silicon nitride / silicon oxide platform. *Optics Express*, 15(11):6846–6856, May 2007.

[8] L. P Biró, Zs Bálint, K. Kertész, Z. Vértesy, G. I Márk, Z. E Horváth, J. Balázs, D. Méhn, I. Kiricsi, V. Lousse, and J. -P Vigneron. Role of photonic-crystal-type structures in the thermal regulation of a lycaenid butterfly sister species pair. *Phys. Rev. E*, 67(2):021907, February 2003.

[9] Matthew Borselli, Thomas J. Johnson, and Oskar Painter. Beyond the rayleigh scattering limit in high-Q silicon microdisks: theory and experiment. *Optics Express*, 13:1515, March 2005.

[10] R.W. Boyd and B.R. Masters. Nonlinear optics. *Journal of Biomedical Optics*, 14:029902, 2009.

[11] T. Carmon and K. J Vahala. Visible continuous emission from a silica microphotonic device by third-harmonic generation. *Nature Physics*, 3(6):430435, 2007.

[12] Alongkarn Chutinan and Susumu Noda. Waveguides and waveguide bends in two-dimensional photonic crystal slabs. *Physical Review B*, 62(7):4488, 2000.

[13] R. Cocciol, M. Boroditsky, K. W Kim, Y. Rahmat-Samii, and E. Yablonovitch. Smallest possible electromagnetic mode volume in a dielectric cavity. *IEE Proc. Optoelectronics*, 145:391–397, 1998.

[14] D. Correia, J. P. da Silva, and H. E. Hernandez-Figueroa. Genetic algorithm and finite-element design of short single-section passive polarization converter. *IEEE Photonics Technology Letters*, 15(7):915917, 2003.

[15] N. Daldosso, M. Melchiorri, F. Riboli, F. Sbrana, L. Pavesi, G. Pucker, C. Kompocholis, M. Crivellari, P. Bellutti, and A. Lui. Fabrication and optical characterization of thin two-dimensional Si3N4 waveguides. *Materials Science in Semiconductor Processing*, 7(4-6):453–458, 2004.

[16] P. DelHaye, A. Schliesser, O. Arcizet, T. Wilken, R. Holzwarth, and T. J. Kippenberg. Optical frequency comb generation from a monolithic microresonator. 2007.

[17] E Desurvire. Capacity demand and technology challenges for lightwave systems in the next two decades. *Lightwave Technology, Journal of*, 24(12):4697–4710, 2006.

[18] Shanhui Fan, Joshua N Winn, Adrian Devenyi, J. C Chen, Robert D Meade, and J. D Joannopoulos. Guided and defect modes in periodic dielectric waveguides. *JOSA*, 12, 1994.

[19] Eyal Feigenbaum and Meir Orenstein. Optical 3D cavity modes below the diffraction-limit using slow-wave surface-plasmon-polaritons. *Optics Express*, 15:2607–2612, March 2007.

[20] Kevin Foubert, Loic Lalouat, Benoit Cluzel, Emmanuel Picard, David Peyrade, Eric Delamadeleine, Frederique de Fornel, and Emmanuel Hadji. Near-field modal microscopy of subwavelength light confinement in multimode silicon slot waveguides. *Applied Physics Letters*, 93(25):251103–3, December 2008.

[21] S. Gaugiran, S. Gtin, J. Fedeli, G. Colas, A. Fuchs, F. Chatelain, and J. Drouard. Optical manipulation of microparticles and cells on silicon nitride waveguides. *Optics Express*, 13(18):6956–6963, 2005.

[22] B. Gayral, J. M. Gerard, A. Lemaitre, C. Dupuis, L. Manin, and J. L. Pelouard. High-Q wet-etched GaAs microdisks containing InAs quantum boxes. *Applied Physics Letters*, 75(13):1908–1910, 1999.

[23] Alexander Gondarenko and Michal Lipson. Low modal volume dipole-like dielectric slab resonator. *Optics Express*, 16(22):17689–17694, October 2008.

[24] Alexander Gondarenko, Stefan Preble, Jacob Robinson, Long Chen, Hod Lipson, and Michal Lipson. Spontaneous emergence of periodic patterns in a biologically inspired simulation of photonic structures. *Physical Review Letters*, 96:143904, April 2006.

[25] N. A. Gondarenko, S. L. Ossakow, and G. M. Milikh. Generation and evolution of density irregularities due to self-focusing in ionospheric modifications. *Journal of Geophysical Research-Space Physics*, 110(A9):A09304, 2005.

[26] A. Gorin, A. Jaouad, E. Grondin, V. Aimez, and P. Charette. Fabrication of silicon nitride waveguides for visible-light using PECVD: a study of the effect of plasma frequency on optical properties. *Optics Express*, 16(18):13509–13516, 2008.

[27] P. L. Gourley, J. R. Wendt, G. A. Vawter, T. M. Brennan, and B. E. Hammons. Optical properties of two-dimensional photonic lattices fabricated as honeycomb nanostructures in compound semiconductors. *Applied Physics Letters*, 64(6):687–689, February 1994.

[28] Ivan S. Grudinin, Nan Yu, and Lute Maleki. Generation of optical frequency combs with a CaF2 resonator. *Optics Letters*, 34(7):878–880, April 2009.

[29] Junpeng Guo, M.J. Shaw, G. Allen Vawter, P. Esherick, G. Ronald Hadley, and C.T. Sullivan. High-Q integrated on-chip micro-ring resonator. In *Lasers and Electro-Optics Society, 2004. LEOS 2004. The 17th Annual Meeting of the IEEE*, volume 2, pages 745–746 Vol.2, 2004.

[30] John H. Holland. *Adaptation in natural and artificial systems. an introductory analysis with applications to biology, control and artificial intelligence*. 1975.

[31] Ehsan Shah Hosseini, Siva Yegnanarayanan, Mohammad Soltani, and Ali Adibi. Ultra-high quality factor microdisk resonators for chip-scale visible integrated photonics. In *Frontiers in Optics*, page FMG4. Optical Society of America, 2008.

[32] Kazuhiro Ikeda, Robert E. Saperstein, Nikola Alic, and Yeshaiahu Fainman. Thermal and kerr nonlinear properties of plasma-deposited silicon nitride/ silicon dioxide waveguides. *Optics Express*, 16(17):12987–12994, 2008.

[33] J. Jiang, J. Cai, G. P Nordin, and L. Li. Parallel microgenetic algorithm design for photonic crystal and waveguide structures. *Optics letters*, 28(23):23812383, 2003.

[34] J. D Joannopoulos, S. G Johnson, and J. N Winn. *Photonic crystals: molding the flow of light*. Princeton university press, 2008.

[35] Steven G. Johnson, Shanhui Fan, Pierre R. Villeneuve, J. D. Joannopoulos, and L. A. Kolodziejski. Guided modes in photonic crystal slabs. *Physical Review B*, 60(8):5751, 1999.

[36] J.S. Kilby. Invention of the integrated circuit. *Electron Devices, IEEE Transactions on*, 23(7):648–654, 1976.

[37] S. Kim, G. P Nordin, J. Cai, and J. Jiang. Ultracompact high-efficiency polarizing beam splitter with a hybrid photonic crystal and conventional waveguide structure. *Optics letters*, 28(23):23842386, 2003.

[38] T. J. Kippenberg, S. M. Spillane, and K. J. Vahala. Kerr-nonlinearity optical parametric oscillation in an ultrahigh-Q toroid microcavity. *Physical review letters*, 93(8):83904, 2004.

[39] Mahito Kohmoto, Bill Sutherland, and K. Iguchi. Localization of optics: Quasiperiodic media. *Physical Review Letters*, 58(23):2436, June 1987.

[40] John R. Koza, Martin A. Keane, Matthew J. Streeter, William Mydlowec, Jessen Yu, and Guido Lanza. *Genetic Programming IV: Routine Human-Competitive Machine Intelligence*. Springer, July 2003.

[41] Soon-Hong Kwon, Thomas Snner, Martin Kamp, and Alfred Forchel. Optimization of photonic crystal cavity for chemical sensing. *Optics Express*, 16:11709, July 2008.

[42] F. Van Laere, M. Ayre, D. Taillaert, D. Van Thourhout, T. F. Krauss, and R. Baets. Compact and efficient fibre-to-waveguide grating couplers in InP-membrane. *Electronics Letters*, 42(6):343345, 2006.

[43] B. G Lee, A. Biberman, A. C Turner-Foster, M. A Foster, M. Lipson, A. L Gaeta, and K. Bergman. Demonstration of broadband wavelength conversion at 40 gb/s in silicon waveguides. *IEEE Photonics Technology Letters*, 21(3), 2009.

[44] Hod Lipson and Jordan B. Pollack. Automatic design and manufacture of robotic lifeforms. *Nature*, 406(6799):974–978, 2000.

[45] X. Liu and Y. Li. Optimizing the bandwidth and noise performance of distributed multi-pump raman amplifiers. *Optics Communications*, 230(4-6):425431, 2004.

[46] Marko Loncar, Axel Scherer, and Yueming Qiu. Photonic crystal laser sources for chemical detection. *Applied Physics Letters*, 82:4648, June 2003.

[47] Stefan Maier. Effective mode volume of nanoscale plasmon cavities. *Optical and Quantum Electronics*, 38(1):257–267, 2006.

[48] S. Manos and L. Poladian. Multi-objective and constrained design of fibre bragg gratings using evolutionary algorithms. *Opt. Eng*, 42:28562860, 2003.

[49] Robert D. Meade, Karl D. Brommer, Andrew M. Rappe, and J. D. Joannopoulos. Existence of a photonic band gap in two dimensions. *Applied Physics Letters*, 61(4):495–497, July 1992.

[50] P. Michler, A. Kiraz, C. Becher, W. V. Schoenfeld, P. M. Petroff, Lidong Zhang, E. Hu, and A. Imamoglu. A quantum dot Single-Photon turnstile device. *Science*, 290:2282–2285, December 2000.

[51] J. N. Milgram, J. Wojcik, P. Mascher, and A. P. Knights. Optically pumped si nanocrystal emitter integrated with low loss silicon nitride waveguides. *Optics Express*, 15(22):14679–14688, October 2007.

[52] Melanie Mitchell. *An Introduction to Genetic Algorithms*. The MIT Press, February 1998.

[53] O. Painter, R. K Lee, A. Scherer, A. Yariv, J. D OBrien, P. D Dapkus, and

I. Kim. Two-dimensional photonic band-gap defect mode laser. *Science*, 284, 1999.

[54] A. R Parker, R. C McPhedran, D. R McKenzie, L. C Botten, and N. A.P Nicorovici. Photonic engineering: Aphrodite's iridescence. *NATURE-LONDON-*, page 3636, 2001.

[55] C. R Pollock and M. Lipson. *Integrated photonics*. Kluwer Academic Publishers, 2003.

[56] S. Preble, M. Lipson, and H. Lipson. Two-dimensional photonic crystals designed by evolutionary algorithms. *Applied Physics Letters*, 86:061111, 2005.

[57] E. M. Purcell, H. C. Torrey, and R. V. Pound. Resonance absorption by nuclear magnetic moments in a solid. *Physical Review*, 69:37–38, 1946.

[58] Jacob T. Robinson, Christina Manolatou, Long Chen, and Michal Lipson. Ultrasmall mode volumes in dielectric optical microcavities. *Physical Review Letters*, 95(14):143901, 2005.

[59] L. Sanchis, A. Hakansson, D. Lopez-Zanon, J. Bravo-Abad, and Jose Sanchez-Dehesa. Integrated optical devices design by genetic algorithm. *Applied Physics Letters*, 84(22):4460–4462, May 2004.

[60] A. A Savchenkov, A. B Matsko, D. Strekalov, M. Mohageg, V. S Ilchenko, and L. Maleki. Low threshold optical oscillations in a whispering gallery mode CaF_ $$2$$ resonator. *Physical review letters*, 93(24):243905, 2004.

[61] Jacob Scheuer, William M. J. Green, Guy DeRose, and Amnon Yariv. Low-threshold two-dimensional annular bragg lasers. *Optics Letters*, 29(22):2641–2643, November 2004.

[62] Ali Serpengzel. Amorphous silicon nitride microcavities. *Journal of the Optical Society of America B*, 18(7):989–993, July 2001.

[63] M. Shaw, Junpeng Guo, Allen Vawter, Scott Habermehl, and Charles Sullivan. Fabriaction techniques for low loss silicon nitride waveguides. In *SPIE Proceedigns 5720*, 2005.

[64] Linfang Shen, Zhuo Ye, and Sailing He. Design of two-dimensional pho-

tonic crystals with large absolute band gaps using a genetic algorithm. *Physical Review B*, 68(3):035109, July 2003.

[65] Bong-Shik Song, Susumu Noda, Takashi Asano, and Yoshihiro Akahane. Ultra-high-Q photonic double-heterostructure nanocavity. *Nat Mater*, 4(3):207–210, March 2005.

[66] M. M Spuhler, B. J Offrein, G. L Bona, R. Germann, I. Massarek, and D. Erni. A very short planar silica spot-size converter using a nonperiodic segmented waveguide. *Journal of Lightwave Technology*, 16(9):16801685, 1998.

[67] Allen Taflove and Susan C. Hagness. *Computational Electrodynamics: The Finite-Difference Time-Domain Method, Third Edition*. Artech House Publishers, 3 edition, June 2005.

[68] D. Taillaert, P. Bienstman, and R. Baets. Compact efficient broadband grating coupler for silicon-on-insulator waveguides. *Optics letters*, 29(23):27492751, 2004.

[69] D. Taillaert, W. Bogaerts, P. Bienstman, T. F. Krauss, P. Van Daele, I. Moerman, S. Verstuyft, K. De Mesel, and R. Baets. An out-of-plane grating coupler for efficient butt-coupling betweencompact planar waveguides and single-mode fibers. *IEEE Journal of Quantum Electronics*, 38(7):949955, 2002.

[70] Takasumi Tanabe, Masaya Notomi, Eiichi Kuramochi, and Hideaki Taniyama. Large pulse delay and small group velocity achieved using ultrahigh-Q photonic crystal nanocavities. *Optics Express*, 15:7826–7839, June 2007.

[71] Takasumi Tanabe, Akihiko Shinya, Eiichi Kuramochi, Shingo Kondo, Hideaki Taniyama, and Masaya Notomi. Single point defect photonic crystal nanocavity with ultrahigh quality factor achieved by using hexapole mode. *Applied Physics Letters*, 91:1110, July 2007.

[72] K. J Vahala. Optical microcavities. *Nature*, 424(6950):839846, 2003.

[73] P. Velha, E. Picard, T. Charvolin, E. Hadji, J. C. Rodier, P. Lalanne, and D. Peyrade. Ultra-High Q/V Fabry-Perot microcavity on SOI substrate. *Optics Express*, 15:16090, 2007.

[74] Laurent Vivien, Delphine Marris-Morini, Amadeu Griol, Kristinn B. Gylfason, Daniel Hill, Jes Alvarez, Hans Sohlstr?m, Juan Hurtado, David Bou-

ville, and Eric Cassan. Vertical multiple-slot waveguide ring resonators in silicon nitride. *Optics Express*, 16(22):17237–17242, October 2008.

[75] R. Waldausl, B. Schnabel, E. B Kley, and A. Brauer. Efficient focusing polymer waveguide grating couplers. *Electronics Letters*, 33(7):623624, 1997.

[76] B. Wang, J. Jiang, D. M Chambers, J. Cai, and G. P Nordin. Stratified waveguide grating coupler for normal fiber incidence. *Optics letters*, 30(8):845847, 2005.

[77] B. Wang, J. Jiang, and G. P. Nordin. Embedded slanted grating for vertical coupling between fibers and silicon-on-insulator planar waveguides. *IEEE Photonics Technology Letters*, 17(9):18841886, 2005.

[78] Diederik S. Wiersma, Paolo Bartolini, Ad Lagendijk, and Roberto Righini. Localization of light in a disordered medium. *Nature*, 390(6661):671–673, December 1997.

[79] Qianfan Xu, Vilson R. Almeida, Roberto R. Panepucci, and Michal Lipson. Experimental demonstration of guiding and confining light in nanometer-sizelow-refractive-index material. *Optics Letters*, 29(14):1626–1628, July 2004.

[80] Eli Yablonovitch. Inhibited spontaneous emission in Solid-State physics and electronics. *Physical Review Letters*, 58(20):2059, May 1987.

[81] Kane Yee. Numerical solution of inital boundary value problems involving maxwell's equations in isotropic media. *Antennas and Propagation, IEEE Transactions on*, 14(3):302–307, 1966.